OULU 2025
C 1013

ACTA
UNIVERSITATIS OULUENSIS

Aidin Heidari

HYDROGEN REDUCTION OF INDUSTRIAL IRON ORE PELLETS

A MULTI-SCALE STUDY FROM SURFACE TO CORE

UNIVERSITY OF OULU GRADUATE SCHOOL;
UNIVERSITY OF OULU,
FACULTY OF TECHNOLOGY

ACTA UNIVERSITATIS OULUENSIS
C Technica 1013

AIDIN HEIDARI

HYDROGEN REDUCTION OF INDUSTRIAL IRON ORE PELLETS

A multi-scale study from surface to core

Academic dissertation to be presented with the assent of the Doctoral Programme Committee of Technology and Natural Sciences of the University of Oulu for public defence in the Oulun Puhelin auditorium (L5), Linnanmaa, on 29 August 2025, at 12 noon

UNIVERSITY OF OULU, OULU 2025

Acta Univ. Oul. C 1013, 2025

Supervised by
Professor Timo Fabritius
Doctor Mikko Iljana
Doctor Anne Hietava

Reviewed by
Professor Jafar Safarian
Associate Professor Leili Tafaghodi

Opponent
Docent Mikko Helle

ISBN 978-952-62-4544-7 (Paperback)
ISBN 978-952-62-4545-4 (PDF)

ISSN 0355-3213 (Printed)
ISSN 1796-2226 (Online)

Cover Design
Raimo Ahonen

PUNAMUSTA
TAMPERE 2025

Heidari, Aidin, Hydrogen reduction of industrial iron ore pellets. A multi-scale study from surface to core
University of Oulu Graduate School; University of Oulu, Faculty of Technology
Acta Univ. Oul. C 1013, 2025
University of Oulu, P.O. Box 8000, FI-90014 University of Oulu, Finland

Abstract

The transition towards sustainable ironmaking necessitates the replacement of carbon-based reduction processes with hydrogen-based alternatives to mitigate CO_2 emissions. This study investigates the reduction behavior of two types of industrial pellets utilized in direct reduction (DRI) and blast furnaces (BFs), using hydrogen (H_2) and carbon monoxide (CO) as reducing agents. The experimental analysis utilizes ambient pressure X-ray photoelectron spectroscopy (APXPS) to examine the surface reduction mechanisms and a thermogravimetric analysis (TGA) to evaluate kinetic parameters in bulk scale.

DRI pellets achieved a higher metallization degree during surface reduction by hydrogen due to their higher porosity. Although adding CO to the reducing gas hindered the formation of metallic iron in DRI pellet, BF pellet reached to 20% metallization degree by a mixture of 50:50 $CO:H_2$. However, subsequent reoxidation of the reduced iron to wüstite and magnetite occurred due to increasing partial pressure of H_2O and CO_2 on the surface of the pellets.

Investigating the effect of water vapor on the hydrogen reduction of pellets showed that although complete reduction is thermodynamically possible with 30% water vapor in the system, the reduction of wüstite to iron could not start, even at high temperatures, due to a kinetic barrier. The effect of 20% water vapor on the reduction degree was dependent on the reduction temperature. Although adding 10% water vapor decreased the rate of reduction, it did not affect the reduction degree.

Keywords: APXPS, hydrogen, iron ore pellet, reduction rate, reduction

Heidari, Aidin, Teollisuuden rautamalmipellettien vetypelkistys. Moniasteikkoinen pinnalta ytimeen -tutkimus
Oulun yliopiston tutkijakoulu; Oulun yliopisto, teknillinen tiedekunta
Acta Univ. Oul. C 1013, 2025
Oulun yliopisto, PL 8000, 90014 Oulun yliopisto

Tiivistelmä

Siirtyminen kestävään raudanvalmistukseen edellyttää hiilipohjaisten pelkistysprosessien korvaamista vetyyn perustuvilla vaihtoehdoilla hiilidioksidipäästöjen vähentämiseksi. Tämä tutkimus tarkastelee kahden teollisen pellettityypin pelkistymiskäyttäytymistä suorapelkistyksessä (DRI) ja masuunissa (BF) käyttäen pelkistimenä vetyä (H_2) ja hiilimonoksidia (CO). Kokeellinen analyysi hyödyntää painetta kontrolloivaa röntgenfotoelektronispektroskopiaa (APXPS) pinnan pelkistysmekanismien tutkimiseen sekä termogravimetristä analyysia (TGA) kineettisten parametrien arviointiin suuremmassa mittakaavassa.

Tutkittaessa pinnan pelkistymistä vedyllä DRI-pelletti saavutti korkeamman metallisaatioasteen verrattuna BF-pellettiin, mikä johtui sen suuremmasta huokoisuudesta. Metallista rautaa ei muodostunut DRI-pelletissä, kun pelkistyskaasuun vedyn lisäksi lisättiin hiilimonoksidia. Kuitenkin BF-pelletti saavutti korkeamman metallisaatioasteen (20 %), kun pelkistyskaasujen suhde oli 50:50. Pelkistyneen raudan uudelleenhapettumista wüstiitiksi ja magnetiitiksi havaittiin tapahtuvan, kun H_2O- ja CO_2-osapaineet kasvoivat pelletin pinnalla.

Tutkittaessa vesihöyryn vaikutusta pelletin vetypelkistyksen aikana havaittiin, että vaikka täydellinen pelkistyminen on termodynaamisesti mahdollista vesihöyrypitoisuuden ollessa 30 %, wüstiitin pelkistyminen raudaksi ei tapahdu edes korkeissa lämpötiloissa kineettisten esteiden takia. Vesihöyrypitoisuuden ollessa 20 % pelkistymiseen vaikutti myös käytetty pelkistyslämpötila. Vaikka 10 prosentin vesihöyrypitoisuus hidasti pelkistysnopeutta, se ei vaikuttanut pelkistysasteeseen.

Asiasanat: APXPS, pelkistysnopeus, rautamalmipelletit, vetypelkistys

Dedicated to those who have strived for freedom, in thought, in spirit, and in life.

Acknowledgements

I would like to express my deepest gratitude to my main supervisor, Professor Timo Fabritius, for his unwavering trust in me and for giving me the opportunity to join the University of Oulu from 5000 kilometers away. His exceptional guidance, leadership, and support have been invaluable throughout this journey.

I am also sincerely grateful to my co-supervisors, Dr. Mikko Iljana and Dr. Anne Hietava, for their constant support and encouragement, which have been instrumental in helping me complete my PhD. Additionally, I extend my appreciation to Riku Mattila, Laboratory Manager, and Tommi Kokkonen, Project Researcher, for their invaluable technical assistance.

I acknowledge the Centre for Material Analysis (CMA) and MAX IV Laboratory for providing essential laboratory and characterization facilities that significantly contributed to this research.

This work was made possible by the generous support of the Sustainable Hydrogen—Potential for Bothnia Gulf Cluster project (20357962), funded by the European Regional Development Fund (ERDF). I also appreciate the financial and strategic assistance from the FFS2—Towards Fossil-Free Steel 2 (grant number 5534/31/2023) and the CLEAN2STEEL project, supported by the Kvantum Institute. A special thanks to the Finnish Foundation for Technology Promotion (Tekniikan Edistämissäätiö) and Tauno Tönning Foundation for their financial support, which has greatly contributed to this research.

Beyond academia, I am deeply thankful to my friends, who have filled these four years with joyful and unforgettable moments, helping me maintain a balance between work and personal life.

Lastly, my heartfelt gratitude goes to my family. Despite the physical distance between us, I have always felt their unwavering love, support, and positive energy in every moment of my journey.

10.2.2025 Aidin Heidari

List of abbreviations and symbols

etc.	et cetera
i.e.	id est
e.g.	exempli gratia
APXPS	Ambient pressure X-ray photoelectron spectroscopy
TGA	Thermogravimetric analysis
FESEM	Field emission scanning electron microscopy
XRD	X-ray diffraction
BF	Blast furnace
DRI	Direct reduced iron
EAF	Electric arc furnace
α	Reaction fraction
SCCM	Standard cubic centimeters per minute
BOF	Basic oxygen furnace
CO	Carbon monoxide
CO_2	Carbon dioxide
Fe_2O_2	Hematite
Fe_3O_4	Magnetite
FeO	Wüstite
η	Gas utilization
K	Equilibrium constant
a	Activity
H_2	Hydrogen
k	Rate constant
E_a	Activation energy
A	Frequency factor
R	Gas constant
T	Temperature in Kelvin
D	Diffusion coefficient
D_0	Maximum diffusion coefficient
H_2O	Water vapor
LOI	Loss on ignition
Fe_{tot}	All the iron content in the sample
SiO_2	Silicium oxide
CaO	Calcium oxide
Al_2O_3	Aluminum oxide

MgO	Magnesium oxide
TiO_2	Titanium oxide
V_2O_5	Vanadium oxide
MnO	Manganese oxide
UHV	Ultra-high vacuum
DSC	Differential scanning calorimetry
$G(\alpha)$	Integral representation of the reaction model
$f(\alpha)$	Differential representation of $G(\alpha)$
$k(T)$	Apparent rate constant
t	Time
m_1	Weight of the sample prior to reduction
m_t	Weight of the sample at reduction time t
m_O	weight of oxygen in the form of iron oxide available for reaction throughout the reduction process
eV	Electron volt
Fe^0	Elemental iron
Fe^{2+}	Ferrous cation
Fe^{3+}	Ferric cation
°C	Degree of Celsius
ΔG	Gibbs free energy
ΔG^0	Standard Gibbs free energy
θ_{H2O}	Fraction of surface sites occupied by water vapor
θ_{H2}	Fraction of surface sites occupied by hydrogen
θ_O	Fraction of surface sites occupied by oxygen
θ_ψ	Fraction of surface sites occupied by activated complex
$\theta_\square$	Fraction of vacant surface sites

List of original publications

This thesis is based on the following publications, which are referred throughout the text by their Roman numerals:

I Heidari, A., Niknahad, N., Iljana, M., & Fabritius, T. (2021). A review on the kinetics of iron ore reduction by hydrogen. *Materials*, *14*(24), 7540. https://doi.org/10.3390/ma14247540

II Heidari, A., Ghosalya, M. K., Alaoui Mansouri, M., Heikkilä, A., Iljana, M., Kokkonen, E., Huttula, M., Fabritius, T., & Urpelainen, S. (2024). Hydrogen reduction of iron ore pellets: A surface study using ambient pressure X-ray photoelectron spectroscopy. *International Journal of Hydrogen Energy*, *83,* 148–161. https://doi.org/10.1016/j.ijhydene.2024.08.094

III Heidari, A., Heikkilä, A., Iljana, M., & Fabritius, T. (2024). A comparison between the reduction behavior of DRI and BF pellets in H_2 and CO atmospheres. *Journal of Sustainable Metallurgy*, *10*(4), 2068–2084. https://doi.org/10.1007/s40831-024-00951-x

IV Heidari, A., Ilmakangas, T., Pöyhtäri, S., Heikkinen, E. P., Sulasalmi, P., & Fabritius, T. (In press). The influence of water vapor on hydrogen reduction of iron ore pellets. *Ironmaking & Steelmaking*.

Contents

Abstract
Tiivistelmä

Acknowledgements **9**
List of abbreviations and symbols **11**
List of original publications **13**
Contents **15**
1 Introduction **17**
1.1 Thermodynamics of reduction ... 19
1.2 The kinetics of reduction ... 24
1.2.1 The effect of temperature ... 25
1.2.2 The effect of the gas flow rate ... 26
1.2.3 The effect of particle size and porosity ... 27
1.2.4 The effect of pressure ... 27
1.2.5 The effect of mineralogy of iron ... 28
1.2.6 The effect of impurities ... 29
2 Materials and methods **31**
2.1 Materials ... 31
2.1.1 Iron ore pellets ... 31
2.2 Methods ... 31
2.2.1 Ambient pressure X-ray photoelectron spectroscopy (APXPS) ... 32
2.2.2 Thermogravimetric analysis (TGA) ... 33
2.2.3 Optical microscopy ... 34
2.2.4 Field emission scanning electron microscopy (FESEM) ... 34
2.2.5 X-Ray diffraction (XRD) ... 35
2.2.6 Micro-CT ... 35
2.2.7 HSC Chemistry ... 35
2.2.8 Kinetics analysis method ... 35
3 Results **37**
3.1 The surface reduction of iron ore pellets ... 37
3.2 The bulk reduction of iron ore pellets ... 43
3.3 The effect of water vapor on the hydrogen reduction of iron ore pellets ... 50
4 Discussion **57**
4.1 Comparison between DRI and BF pellets ... 57

4.1.1 Reduction and microstructure 57
4.1.2 Kinetic analysis 65
4.2 The effect of water vapor on the reduction 68
4.2.1 Reduction and microstructure 68
4.2.2 Kinetic analysis 69
5 Conclusion 77
5.1 Conclusion 77
5.2 Future work 78
List of references 81
Original publications 89

1 Introduction

The iron and steel industry is one of the most important industries and plays an undeniable role in the global economy with a major effect on many other industries. At present, the global steel industry heavily relies on the conventional blast furnace (BF) and basic oxygen furnace (BOF) methods to produce approximately 70% of all crude steel. These methods involve the utilization of coke as a primary source for carbon monoxide (CO) generation, which serves as the key reducing agent. Regrettably, this traditional approach contributes to the release of approximately 1.9 metric tons of carbon dioxide (CO_2) for each ton of steel produced, posing significant environmental concerns (Souza Filho et al., 2022). The remaining 30% of steel production is achieved using electric arc furnaces (EAF), where steel scrap and directly reduced iron (DRI) are melted. In the direct reduction process, carbon monoxide (CO) and hydrogen (H_2) are generated as the reducing agents through the high-temperature decomposition of natural gas. Although this route results in significantly lower CO_2 emissions compared to the blast furnace method, the continued use of CO as a reducing agent in direct reduction processes remains a source of concern in relation to CO_2 emissions (Souza Filho et al., 2021). It is worth noting that the iron and steel industries collectively contribute to approximately 7% of the global total CO_2 emissions, emphasizing the need for sustainable and low-carbon steel production methods (Heidari et al., 2021). Therefore, researchers and industries are looking for alternative technologies to lower CO_2 emission and to make the process more environmentally friendly.

In the context of metallurgical processes, green hydrogen offers a sustainable alternative for reducing iron ore. The utilization of hydrogen in direct reduction processes can substantially lower the carbon footprint of steel production. Recent studies have demonstrated the feasibility of hydrogen-based reduction at various temperatures, highlighting its potential to revolutionize the steel industry (Hölling & Gellert, 2018; S. Li et al., 2021).

Using hydrogen as a reducing agent has been considered the main alternative for the transition to fossil-free ironmaking (Rukini et al., 2022; R. R. Wang et al., 2021). Hydrogen can be utilized in three different ways. First, injecting hydrogen into the blast furnace. In this method, part of the coke (CO as the reducing gas) is replaced by hydrogen, which mitigates CO_2 emission. However, since the blast furnace has been designed to operate with coke, it is not possible to replace all of the coke with hydrogen (Yilmaz et al., 2017). The second method is direct reduction (DR) using hydrogen as a reducing gas that can be done in shaft furnaces or fluidized bed reactors. This process can be achieved with only hydrogen, which can be fossil-free if the hydrogen is produced through methods such as water electrolysis (Spreitzer & Schenk, 2019a; L. Wang et al., 2022). The third method is plasma hydrogen reduction in which iron ore can be melted and reduced simultaneously in a plasma arc zone (Raabe et al., 2023).

Among the mentioned routes, direct hydrogen reduction is closer to scaling up and industrialization and some companies have started to design plants (Kushnir et al., 2020). However, the feasibility of completely shutting down all existing blast furnaces worldwide and swiftly replacing them with hydrogen-based shaft furnaces is impractical. Therefore, many industries view the injection of hydrogen into existing blast furnaces as a short-term solution (Sun et al., 2023). The thermodynamics and kinetics of the process have been widely studied by researchers. Studies show that the reduction of iron ore by hydrogen is considerably faster than the reduction by carbon monoxide (Heidari et al., 2021; S. Li et al., 2022). Hydrogen can diffuse faster because of its small molecular size and higher mobility, and it has higher reaction rates. However, since the hydrogen reduction is endothermic, the required energy should be supplied by an external source. The hydrogen reduction process can be comprehensively studied on three distinct scales: macroscopic, mesoscopic, and microscopic. Macroscopic investigations offer insights into transport phenomena and reaction kinetics within shaft furnaces, while the mesoscopic scale is apt for exploring the structural evolution of iron ore pellets during the reduction process. However, it is at the microscopic scale that we gain access to invaluable information pertaining to crystal defects, interfacial reactions, porosity, chemical composition variations, and mechanical factors that can significantly impact the overall kinetics of the process.

This doctoral thesis provides an in-depth review of the kinetics involved in the hydrogen reduction of iron ore, covered in the first supplement. The primary goal of this literature review was to compile findings and methodologies from various studies to identify key parameters influencing reduction kinetics and to highlight areas needing further investigation. Following the review, two types of iron ore pellets, differing in chemical composition and physical characteristics, were selected for detailed study. The reduction behavior of these pellets was examined both at the surface and in the bulk. Surface-level reduction was analyzed using APXPS, with results presented in Publication II. Bulk reduction was studied in Publication III, using single pellet reduction tests in a TGA at various temperatures. Given the significance of water vapor, which is inherently present during reduction yet understudied, its effect on hydrogen reduction of iron ore pellets was specifically explored in Publication IV.

In this study, the reduction process was examined at a depth very close to the surface for the first time. Additionally, bulk reduction experiments using two types of industrial pellets and a broad range of temperatures and water vapor levels (up to 30%) provided valuable industrial relevance and insight.

In Figure 1, the publications are presented graphically, and how they relate to the thesis goal. The main focus is on pellets, as previously stated, and this emphasis is clearly shown in Figure 1.

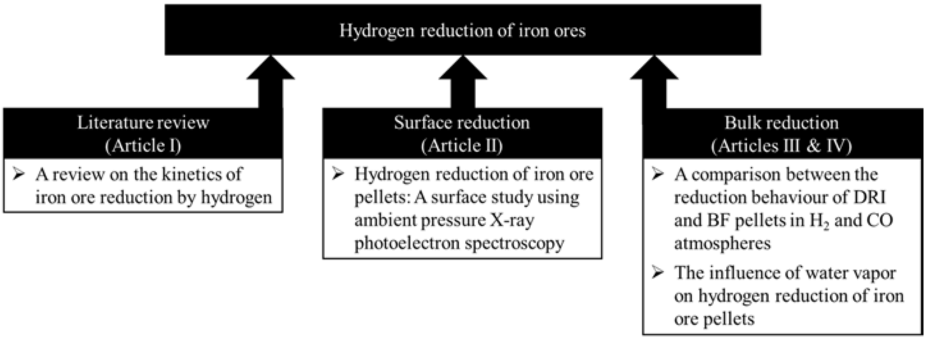

Fig. 1. Structure of thesis and published articles.

1.1 Thermodynamics of reduction

Iron oxide is in the forms of Fe_2O_3 (hematite), Fe_3O_4 (magnetite), and FeO (wüstite). However, wüstite is not stable at temperatures lower than 570 °C and it is formed during a reduction process at temperatures higher than 570 °C. A direct reaction between iron oxide and carbon does not occur in the blast furnace due to the very slow kinetics, because the two reactants are in solid phases. Hence, carbon first reacts with oxygen and produces carbon monoxide according to the reaction (1), which is the reducing agent. Carbon monoxide also can be produced by reforming the natural gas in direct reduction plants as follows

$$C\ (s) + {}^{1}/_{2}\ O_2\ (g) = CO\ (g). \tag{1}$$

Iron oxide can be reduced to metallic iron by carbon monoxide, according to the following reactions:

$$3\ Fe_2O_3\ (s) +\ CO\ (g) = 2\ Fe_3O_4\ (s) + CO_2\ (g), \tag{2}$$

$$Fe_3O_4\ (s) + 4\ CO\ (g) = 3\ Fe\ (s) + 4CO_2\ (g) \quad below\ 570℃, \tag{3}$$

$$Fe_3O_4\ (s) + CO\ (g) = 3\ FeO\ (s) + CO_2\ (g) \quad above\ 570℃, \tag{4}$$

and

$$FeO\ (s) + CO\ (g) = Fe\ (s) + CO_2\ (g) \quad above\ 570℃. \tag{5}$$

The overall reduction of hematite to iron can be written as:

$$Fe_2O_3\ (s) + 3\ CO\ (g) = 2\ Fe\ (s) + 3\ CO_2\ (g). \tag{6}$$

All the reactions are exothermic except reduction of magnetite to wüstite. So, the overall reduction does not require extra energy.

The produced CO_2 during reduction reactions is not stable at high temperature and in the presence of C it can transform to CO as in the following reaction, which is called the Boudouard reaction:

$$C\ (s) + CO_2\ (g) = 2\ CO\ (g). \tag{7}$$

The reaction is endothermic and consumes heat. Furthermore, due to Le Chatelier’s principle, at a higher pressure less CO will be produced (Figure 2).

The gas utilization of carbon monoxide can be presented by the parameter η_{CO}, which is the relative amount of CO_2 in the gas mixture

$$\eta_{CO} = \frac{P_{CO_2}}{P_{CO}+P_{CO_2}}. \tag{8}$$

It can be inferred from the equation that when $\eta_{CO}=0$ it means that the gas composition is all CO and reduction is possible, whereas the $\eta_{CO}=1$ shows that there is no CO in the gas mixture and reduction cannot occur. So, the $1-\eta_{CO}$ is the relative amount of CO in the gas mixture.

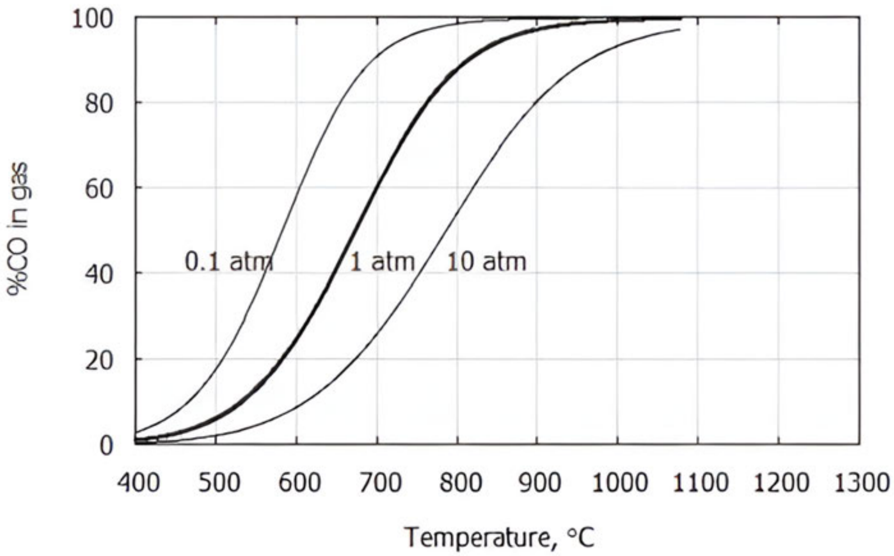

Fig. 2. Stability diagram of a Boudouard reaction at different pressures.

The equilibrium constant for the iron oxide reduction with CO can be written as:

$$\frac{c}{x}\,Fe_xO_y + \left(\frac{c}{x}y - \frac{c}{a}b\right)\,CO = \frac{c}{a}\,Fe_aO_b + \left(\frac{c}{x}y - \frac{c}{a}b\right)\,CO_2 \tag{9}$$

and

$$K = \frac{a_{Fe_aO_b}^{\frac{c}{a}}\,P_{CO_2}^{\left(\frac{c}{x}y-\frac{c}{a}b\right)}}{a_{Fe_xO_y}^{\frac{c}{x}}\,P_{CO}^{\left(\frac{c}{x}y-\frac{c}{a}b\right)}} = \exp\left(-\frac{\Delta G^0}{RT}\right). \tag{10}$$

For pure substances aFe = aFeO = 1.

$$K = \left(\frac{P_{CO_2}}{P_{CO}}\right)^{\left(\frac{c}{x}y-\frac{c}{a}b\right)} \tag{11}$$

and

$$\eta_{CO} = \frac{K}{1+K}. \tag{12}$$

A Baur-Glaessner diagram can be made by plotting 1- η_{CO} versus the temperature. The diagram illustrates the stable regions of iron, wüstite, and magnetite, and the related equilibrium reactions (Figure 3).

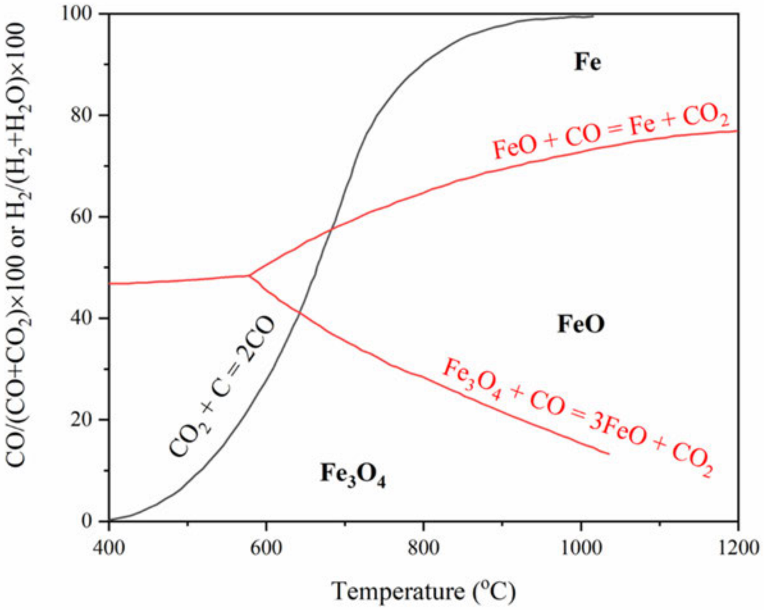

Fig. 3. Baur–Glaessner diagram for an Fe-O-C system (Drawn using HSC Chemistry 10.4.1.1 database).

Reactions 13–16 can be considered for the reduction of iron oxide by hydrogen:

$$3\ Fe_2O_3\ (s) +\ H_2\ (g) = 2\ Fe_3O_4\ (s) + H_2O\ (g), \tag{13}$$

$$Fe_3O_4\ (s) + 4\ H_2\ \ (g) = 3\ Fe\ (s) + 4H_2O\ (g) \quad below\ 570℃, \tag{14}$$

$$Fe_3O_4\ (s) + H_2\ \ (g) = 3\ FeO\ (s) + H_2O\ (g) \quad above\ 570℃, \tag{15}$$

and

$$FeO\ (s) + H_2\ \ (g) = Fe\ (s) + H_2O\ (g) \quad above\ 570℃. \tag{16}$$

The overall reduction of hematite to iron can be written as:

$$Fe_2O_3\ (s) + 3\ H_2\ \ (g) = 2\ Fe\ (s) + 3\ H_2O\ (g). \tag{17}$$

It is clear that the hydrogen reduction of iron oxide is endothermic, and extra energy is needed per mol of iron. This energy should be supplied using supplementary heat from something like the oxidation of hydrogen

$$H_2\ \ (g)\ + \frac{1}{2}\ O_2\ (g) =\ H_2O\ (g). \tag{18}$$

The parameter η_{H2} can be also defined as the gas utilization of hydrogen, which is the relative amount of H_2O in the gas mixture

$$\eta_{H_2} = \frac{P_{H_2O}}{P_{H_2}+P_{H_2O}}. \tag{19}$$

According to the equation, when η_{H2}=0 the gas mixture only contains H_2 and on the other hand when η_{H2}=1 it means that there is only H_2O in the gas mixture. Hence, “1-η_{H2}” can be defined as the relative amount of H_2 in the gas mixture and a measure for the reduction power of the gas mixture, which is called in some literature as “gas quality”. As a result, the reduction reaction is feasible only if η_{H2} lies below a thermodynamic limit.

The equilibrium constant can be calculated as below:

$$\frac{c}{x}\ Fe_xO_y + \left(\frac{c}{x}y - \frac{c}{a}b\right)\ H_2 = \frac{c}{a}\ Fe_aO_b + \left(\frac{c}{x}y - \frac{c}{a}b\right)\ H_2O \tag{20}$$

and

$$K = \frac{a_{Fe_aO_b}^{\frac{c}{a}}\ P_{H_2O}^{\left(\frac{c}{x}y-\frac{c}{a}b\right)}}{a_{Fe_xO_y}^{\frac{c}{x}}\ P_{H_2}^{\left(\frac{c}{x}y-\frac{c}{a}b\right)}} = \exp\left(-\frac{\Delta G^0}{RT}\right). \tag{21}$$

For pure substances $a_{Fe} = a_{FeO} = 1$.

$$K = \left(\frac{P_{H_2O}}{P_{H_2}}\right)^{\left(\frac{c}{x}y-\frac{c}{a}b\right)} \tag{22}$$

and

$$\eta_{H_2} = \frac{K}{1+K} \tag{23}$$

By plotting 1- η_{H2} versus the temperature and adding to Figure 3, the Baur-Glaessner diagram containing Fe-O-C-H system can be plotted as the Figure 4.

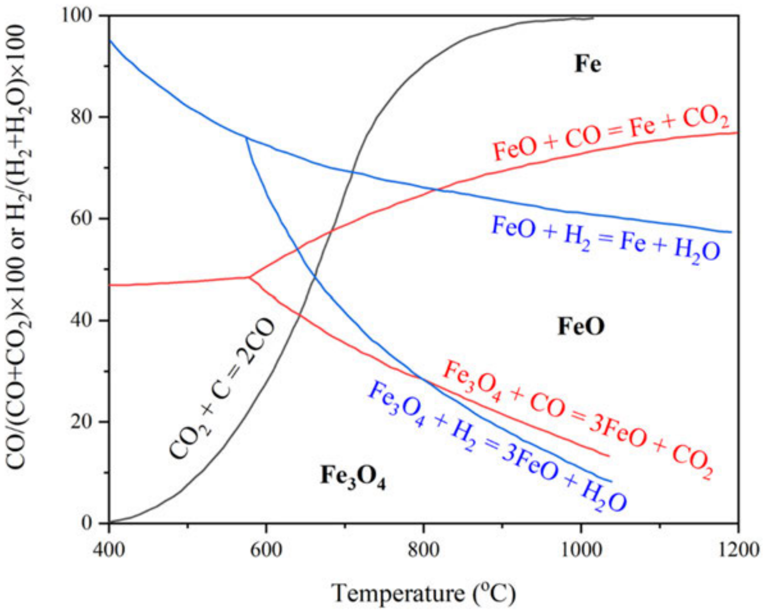

Fig. 4. A Baur–Glaessner diagram for an Fe-O-C-H system (Drawn using HSC Chemistry 10.4.1.1 database) (Modified under CC BY 4.0 license from Publication I and III © 2021, 2024 Authors).

1.2 The kinetics of reduction

The kinetics of the hydrogen-based reduction of iron ores is critical in understanding the efficiency and mechanism of iron production using this environmentally friendly alternatives to traditional carbon-based methods. The kinetics of hydrogen reduction are highly complex, with several factors contributing to this intricacy. While it is widely acknowledged that hydrogen facilitates a faster reduction than carbon monoxide, multiple variables affect the reduction rate (Scharm et al., 2022). These include macrostructural features such as the type of iron oxide (e.g., natural ores or synthesized materials), the morphology of particles (such as lump ore, sinter, pellets, or powders), and their porosity. Additionally, microstructural properties such as the mineral composition, crystal size, and defects, along with experimental conditions such as the temperature, gas flow rate, pressure, and reactor design, all significantly impact the overall reduction kinetics (Heidari et al., 2021).

1.2.1 The effect of temperature

The influence of temperature on reaction kinetics is analyzed from two viewpoints. The temperature dependence of the rate constant is articulated by the Arrhenius equation (Equation 24), where “k” denotes the rate constant, “A” signifies the frequency factor associated with collision frequency and orientation favorability, “E_a” represents the reaction activation energy, “R” is the gas constant, and “T” indicates temperature in Kelvin

$$k = A \exp \frac{-E_a}{RT}. \tag{24}$$

The diffusion coefficient in solids is also temperature-dependent and adheres to the Arrhenius equation (Equation 25). In this context, “D_0” represents the maximum diffusion coefficient, “E_a” denotes the diffusion activation energy, “R” signifies the gas constant

$$D = D_0\, exp \frac{-E_a}{RT}. \tag{25}$$

In both instances, when the temperature rises, the rate of reduction escalates exponentially.

Research indicates that the influence of temperature on the reduction rate is more pronounced at reduction temperatures below 800 °C. Furthermore, at temperatures exceeding 600 °C, the reduction of Fe_2O_3 to Fe_3O_4 occurs rapidly, and elevated temperatures significantly influence the second ($Fe_3O_4 \rightarrow FeO$) and third stages ($FeO \rightarrow Fe$) of the reduction process (H. Chen et al., 2017; X. Mao et al., 2022a). Temperature influences the structure of the direct reduced iron (DRI). A drop in temperature leads to a finer pore structure, whereas an elevation in reduction temperature causes a decrease in the total pore area. Nevertheless, multiple researchers have noted that at reaching a specific temperature threshold, the reaction rate or ultimate reduction degree may decline with additional temperature increases (Bahgat & Khedr, 2007; Piotrowski et al., 2005; Zuo et al., 2015). Certain literature has noted the occurrence of a minimum temperature phenomenon in reduction rates at advanced stages, where the reduction rate reaches a minimum at a specific temperature, subsequently increasing with a higher elevation in the reduction temperature. The reported minimum rate phenomena during the gaseous reduction of iron oxide were elucidated by physical and/or chemical modifications. The emergence of some hard reducible phases, including fayalite and ferrites, along with sintering effects and the α-γ Fe phase transformation at 912 °C, are the primary causes influencing rate minimum events. The diffusion velocity of H_2O or CO_2 in γ-Fe is significantly slower than in α-Fe, leading to a lower rate of reduction at temperatures exceeding 912 °C compared to lower temperatures (Abdel Halim et al., 2023).

Pousette et al. revealed that reduction and carburization reactions in CO + H2 environments are competitive, with carburization predominating at lower temperatures (700 °C) and reduction occurring more rapidly at elevated temperatures (800–900 °C) (Pousette et al., 2024).

1.2.2 The effect of the gas flow rate

The hydrogen flow rate can affect overall concentration of hydrogen in the reactive system. Furthermore, an increased flow rate enhances the diffusion of hydrogen inside the pellet and reduces the resistance to the gaseous diffusion surrounding the particle (Kang et al., 2024a; Ohmi et al., 1983; Ohmi & Usui, 1982). Research indicates that augmenting the gas flow rate often enhances both the reduction rate and the maximum degree of reduction, with a more significant impact observed in the conversion of magnetite to wüstite and wüstite to iron. Additional aspects such as the temperature and characteristics of the pellet can affect the influence of gas flow rate. It has also been found that there exists a critical flow rate, beyond which an increase in flow rate does not significantly affect the reduction rate (Kang et al., 2024a; Kawasaki et al., 1962; Kuila et al., 2016a).

Zhang et al. established that augmenting the fluidizing velocity and hydrogen concentration during the reduction of Chinese hematite ore fines in a fluidized bed transitioned the kinetics model from three-dimensional diffusion to a combination of three-dimensional diffusion and one-dimensional nucleation and growth (J. Zhang et al., 2024). Yu et al. found that an elevated hydrogen concentration positively influenced the reduction rate, and the effect of an H_2 partial pressure fluctuation was substantial even at lower temperatures (D. Yu et al., 2013). Certain research indicates that reducing the gas concentration alters the reduction rate by influencing the adsorption and chemical reaction processes of gas reactants on the surfaces of solid reactants (Monazam et al., 2014; Tang et al., 2021).

1.2.3 The effect of particle size and porosity

Augmenting the particle size consistently diminishes the reduction rate owing to the reduced diffusion distance (F. Chen et al., 2015; Teplov, 2012; Turkdogan & Vinters, 1971; A. Zhang et al., 2020). At low reduction temperatures, the particle size is not a significant characteristic (Corbari & Fruehan, 2010). Furthermore, for particle sizes below a specific threshold, the correlation between the reduction rate and particle size is minimal, as the internal diffusion resistance is negligible in such instances (Hou et al., 2012).

The influence of the dimensions of the iron oxide pellets is also contingent upon their porosity. The effect of size is diminished when the pellets are very porous and amplified when they are less porous. In a more porous particle, the reducing gas can penetrate the particle, allowing reduction to commence simultaneously on all sides. A porous particle contains fewer reactants per unit volume (Wagner et al., 2006).

The reduction rate of iron oxide particles diminishes as the particle size increases. The fractional reduction remains consistent upon completion of the reduction.

Cavaliere et al. examined high-grade Brazilian iron ore pellets at temperatures ranging from 800 to 1000 °C, demonstrating that pore tortuosity impeded gas transport and reduced reaction rates (Cavaliere et al., 2023). Kazemi et al. similarly discovered that although more porous pellets demonstrated accelerated reduction kinetics, the reduction mechanisms were consistent for pellets with comparable hematite content (Kazemi et al., 2017). Conversely, Metolina et al. indicated that porosity exerted a negligible influence on the hydrogen reduction of hematite pellets, while temperature and pellet size were more consequential factors (Metolina et al., 2022). Korobeinikov et al. investigated the effects of the reduction rate and temperature on porosity, demonstrating that slower speeds yielded larger pores, but elevated temperatures and increasing CO concentrations led to coarser pore structures (Korobeinikov et al., 2023).

1.2.4 The effect of pressure

Research has indicated that elevating the absolute pressure while maintaining a constant partial pressure of H_2 does not result in any significant alteration in the decrease rate throughout the initial and intermediate stages. A rise in the partial pressure of H_2 results in an elevated reduction rate. An increased partial pressure of

H_2 correlates with a greater concentration of H_2, which, as posited by other researchers, may elucidate the enhanced reduction rate (Souza Filho et al., 2023).

Özgün et al. highlighted the influence of hydrogen pressure on reduction kinetics and microstructural development during the direct reduction of hematite pellets. Their findings indicated that elevated hydrogen pressure markedly improved the reduction rate and caused considerable alterations in pore shape, resulting in the development of finer grains of metallic iron (Özgün et al., 2024). Kuila et al. observed that a reduction in hydrogen partial pressure from 1 to 0.25 atm resulted in a fall in the final reduction degree from 1.0 to 0.8 (Kuila et al., 2016a).

1.2.5 The effect of mineralogy of iron

The reduction of hematite by hydrogen occurs more rapidly than that of magnetite, particularly at elevated temperatures. This is because of the robust and compact shell of magnetite, which results in reduced diffusivity. Moreover, the greater density of hematite (5.260 g/cm³) relative to magnetite (5.175 g/cm³) results in the formation of micro fractures during the reduction of hematite to magnetite due to volume alteration. In other words, when hexagonal hematite transforms into cubic magnetite, it expands in volume, leading to the formation of cracks and pores. These structural changes enhance the kinetics of magnetite reduction (Kuila et al., 2016a). The created fissures function as porosities, facilitating gas diffusion. Oxy hydroxides such as goethite, FeO(OH), exhibit significant reducibility attributed to the elevated surface area resulting from water loss (Lu et al., 2024).

Angalakuditi et al. emphasized notable disparities in metallization among different iron ores, with hematite and magnetite surpassing goethite and limonite ($FeO(OH).nH_2O$), owing to the latter’s elevated loss on ignition (LOI) (Angalakuditi et al., 2022).

Kar et al. investigated the hydrogen reduction of various bauxite residue pellets and traditional iron ore pellets. The reduction rate of pellets is contingent upon the porosity and grain size of iron complexes, specifically brownmillerite and hematite. The increased porosity and lower hematite particle size in the bauxite residue pellets, along with self-hardened CaO-added bauxite residue, resulted in faster and a greater degree of reduction compared to hematite iron ore pellets (Kar et al., 2023).

1.2.6 The effect of impurities

The incorporation of SiO_2 may result in the formation of iron silicate (fayalite) during reduction. The presence of fayalite adversely impacts the reduction rate, especially in the final stages of reduction (wüstite to iron). The detrimental effect is more significant when the reductant is CO rather than H_2 (Bahgat et al., 2008; Kim et al., 2012).

The majority of the examined investigations indicated a positive impact of CaO on the reduction rate. CaO accelerates reduction by mechanisms such as enhancing the initial porosity, facilitating the dissociation of wüstite, and encouraging a porous structure in the reduced iron layer (Iguchi et al., 1982; Seth & Ross, 1963).

The beneficial effect of Al_2O_3 incorporation on the reduction rate is due to the production of hercynite precipitates. These precipitates are hypothesized to enhance gas diffusion by altering the atomic configuration of the iron oxide structure (Kapelyushin et al., 2015; Shigematsu & Iwai, 1987).

The influence of MgO on the reduction of iron oxides may be advantageous or detrimental, contingent upon the phases that develop during the reduction process. The addition of MgO to magnetite seems to enhance the development of magnesio spinels, therefore encouraging a porous structure. Nonetheless, the addition of MgO to wüstite compacts results in a dense structure due to the creation of magnesio-wüstite (Bahgat et al., 2007; Pan et al., 2018). Teplov et al. observed that both Al_2O_3 and MgO slow down the reduction rate of magnetite by hydrogen, with Al_2O_3 having a stronger inhibitory effect than MgO (Teplov, 2012).

Mishra et al. conducted further research on low-grade multi-metallic magnetite ore pellets and discovered that gangue components such as SiO_2, Al_2O_3, and MgO substantially impacted the porosity and cold crushing strength (CCS), hence influencing the total reduction performance (Mishra et al., 2024).

2 Materials and methods

2.1 Materials

2.1.1 Iron ore pellets

In this research, two types of industrial pellets crucially employed in both direct reduction (DRI) and blast furnace (BF) processes were utilized. Each pellet weighed approximately 8 ± 0.1 grams and measured 15–16 mm in diameter. The selection of these pellets was based on their significance as primary feedstocks in the iron and steel manufacturing industry. The chemical compositions and physical properties of the pellets are detailed in Table 1 and Table 2 respectively. Moreover, XRF has been carried out for each single pellet and the reduction degree has been calculated accurately based on that.

Table 1. The chemical composition of BF and DRI pellets.

Elements		Fe_{tot}	FeO	SiO_2	CaO	MgO	Al_2O_3	TiO_2	V_2O_5	MnO
Mass%	BF	66.7	0.6	1.85	0.43	1.3	0.32	0.35	0.26	-
	DRI	65.79	2.2	3.78	0.73	0.45	0.64	0.23	-	0.028

Table 2. The physical properties of BF and DRI pellets.

Pellet	Bulk density g/cm^3	Crushing strength daN (ISO 4700)
BF	2.2	220
DRI	2.1	190

2.2 Methods

Different devices and software were used to study the reduction behaviour of the pellets and to gain a comprehensive insight. The devices and software that have been utilized in this thesis are listed in Table 3.

Table 3. Devices and software that have been used in the thesis.

Device / software	Application		
	Bulk reduction	Surface reduction	Publication
APXPS		*	(II)
TGA	*		(III) and (IV)
Optical microscopy	*		(III)
FESEM	*	*	(II), (III) and (IV)
XRD	*		(III)
Micro-CT	*		(III)
HSC Chemistry software	*	*	(II), (III) and (IV)
ImageJ software	*		(III)

2.2.1 Ambient pressure X-ray photoelectron spectroscopy (APXPS)

In-situ reduction experiments were conducted at the APXPS end station of the SPECIES beamline at the MAX IV Laboratory in Lund, Sweden (Kokkonen et al., 2021; Urpelainen et al., 2017). A general scheme is illustrated in Figure 5. The SPECIES beamline is a soft X-ray beamline with a photon energy range between 30 and 1500 eV, equipped with a Phoibos 150 hemispherical analyzer. This beamline is suitable for measuring spectra up to 20 mbar and heating up to 1000 °C in an ultra-high vacuum (UHV). Each sample consisted of a slice from a pellet, which was loaded onto a steel plate, and mounted inside the standard cell of the SPECIES APXPS system on a composite PBN/pyrolytic graphite/PBN heater. Carbon monoxide (CO), hydrogen (H_2), and their mixtures were used as reducing gases for the iron ore oxide reduction to see the effect of gas composition on the reduction of both pellets. H_2 and CO gases were dosed through mass flow controllers (MFCs). Before dosing CO and H_2, all the samples were characterized in UHV, and O 1s, C1s, Fe 2p, and Fe 3p spectra were recorded to define the initial compositions. Sample temperatures were measured with a K-type thermocouple. Samples were exposed to different gas mixtures as well as pure CO and H_2. The gas flow rates varied from 0.5 to 10 sccm. The sample temperature was increased sequentially from room temperature to 650 ℃ and kept at each temperature. Considering the experimental conditions such as the gas composition, flow rate, and pressure, reaching a temperature higher than 650 ℃ with the APXPS device in the MAX IV laboratory was not possible. Moreover, since reactions are slower at lower temperatures, monitoring the progress of reduction and the effect of different parameters is easier. The reduction of iron ores at low temperatures has also been studied by other researchers (Adam et al., 1989; Du et al., 2017; P. Li et al., 2022a; Pineau et al., 2006, 2007; Teplov, 2010, 2012).

APXPS measures the kinetic energy of electrons emitted from a material's surface when it is irradiated with X-rays. From this, the binding energies of core electrons are determined, providing X-ray photoelectron spectra. These spectra reveal the elemental composition, chemical states, and bonding environments at the surface, even under near-ambient pressures. APXPS is particularly valuable for observing surface reactions in real time, such as oxidation or reduction processes (Han et al., 2021).

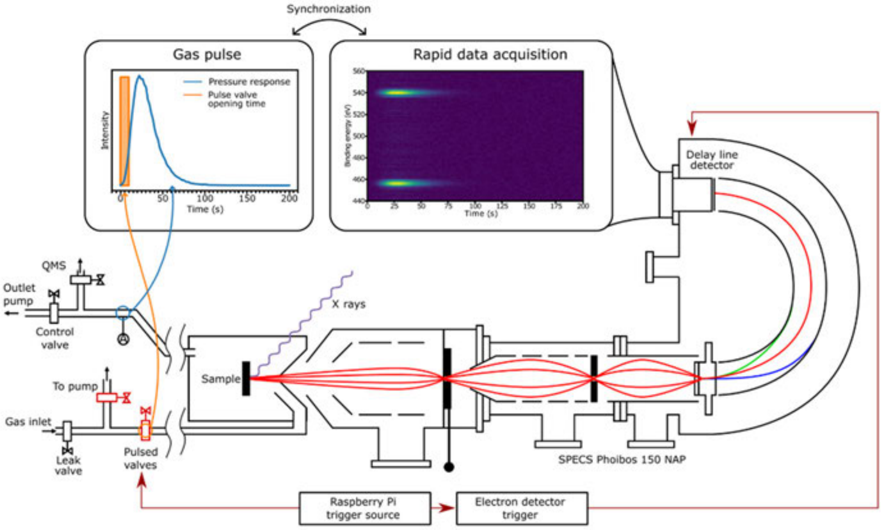

Fig. 5. A schematic of the APXPS cell featuring a sample, gas feeding section, and electron analyzer. Insets display the applied gas perturbation (square pulse) alongside the QMS signal at the cell outlet (left) and the synchronized DLD XPS signal from the sample surface (right), all on the same time scale (Reprinted with permission from Redekop et al., 2021).

2.2.2 Thermogravimetric analysis (TGA)

To ensure the integrity of the samples, the pellets underwent preconditioning in an oven at 120 °C for one hour to eliminate any residual moisture. Subsequently, reduction experiments were conducted utilizing Linseis STA PT 1600, a state-of-the-art Thermogravimetry-Differential Scanning Calorimetry (TG-DSC) device capable of simultaneous mass and heat difference measurements which is illustrated schematically in Figure 6. The device tube is 40 cm in length, and has an inner diameter of 30 mm and a wall thickness of 3 mm. It can work with H_2, CO, CO_2, H_2O, and N_2 up to 1600 °C.

Mass changes have been measured over time using TGA under certain conditions such as temperature, gas flow rate, gas composition, and pressure. The mass change data was then converted to the reduction degree to study the reduction behaviour of pellets in different conditions. Experiments have been repeated twice to minimize the experimental errors.

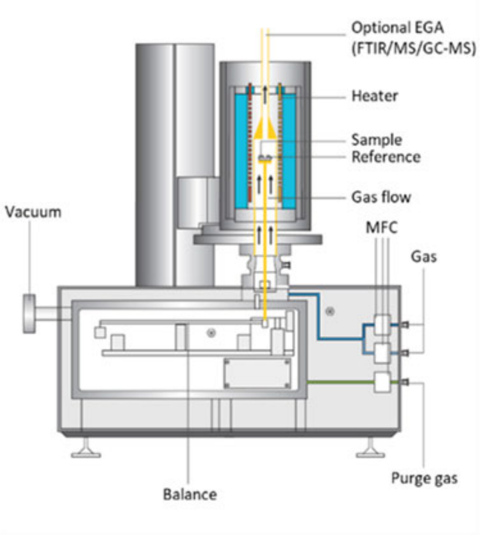

Fig. 6. Schematic of the utilized TG-DSC device (Linseis STA PT 1600) (Modified under CC BY 4.0 license from Publication III and IV © 2024, 2025 Authors).

2.2.3 Optical microscopy

After high-temperature tests, the pellet specimens were embedded in epoxy, subsequently cross-sectioned and polished for analysis. Structural and phase examinations were conducted using an Olympus DSX1000 Digital Microscopes high resolution optical microscope (LOM) to visually inspect the samples.

2.2.4 Field emission scanning electron microscopy (FESEM)

The polished samples were coated with carbon to enhance their conductivity for electron microscopy examination. Morphological investigations of the reduced pellets were then conducted using a field emission scanning electron microscope (FESEM; Zeiss Ultra Plus, Carl Zeiss SMT AG, Germany), coupled with an energy-dispersive X-ray spectroscopy (EDS) device for elemental analysis.

2.2.5 X-Ray diffraction (XRD)

The crystalline phases present in the reduced pellets were identified using an X-ray diffraction (XRD) analysis performed with a Rigaku SmartLab X-ray diffractometer with x-ray radiation source from Co Kα. XRD patterns were recorded over the 2θ-range of 5–130° with a step size of 0.02° and a scanning speed of 4.06 degrees per minute, operating at 40 kV and 135 mA.

To carry out the XRD analysis, samples have been ground into a fine powder using a mortar and pestle, and then the powder has been mounted onto a sample holder.

2.2.6 Micro-CT

X-ray microtomographic imaging at the research unit of medical imaging physics and technology, Faculty of Medicine, University of Oulu was utilized to study the porosity of the pellets.

2.2.7 HSC Chemistry

The Lpp Diagram module of HSC Chemistry 9 software was used to plot Fe–O–C and Fe–O–H phase stability diagrams based on the reaction equations and thermodynamic database. The Lpp Diagram module calculates the phase stability boundaries as lines based on the reaction equations (vector graphics). In other words, the Lpp Diagram module draws isothermal phase stability diagrams of three element systems, also known as predominance area diagrams or Kellogg diagrams.

2.2.8 Kinetics analysis method

The predominant method for ascertaining isothermal kinetics parameters is model fitting. By integrating experimental data and aligning it with established models, the ideal model can be identified among probable candidates based on the minimal deviation in the conversion rate between the experimental data and the model’s computed results.

The rate of the reduction reaction can be determined by distinguishing the degree of the reaction conversion over time. The kinetic equation at this juncture is represented by Equation 26:

$$r = \frac{d\alpha}{dt} = k(T)f(\alpha). \tag{26}$$

In the study of isothermal kinetics, the integral method can be employed for data analysis and processing, as depicted in Equation 27:

$$G(\alpha) = \int_0^\alpha \frac{d\alpha}{f(\alpha)} = \int_0^t k(T)dt = k(T)t, \tag{27}$$

where G(α) denotes the integral representation of the reaction model, f(α) signifies the differential representation of G(α), k(T) indicates the apparent rate constant at the reaction temperature T, and t represents the reaction time. The rate-determining mechanism of the reduction reaction is confirmed using G(α), as each G(α) is constructed from particular reaction steps (including nucleation and nucleus growth, phase interface chemical reaction, or diffusion).

The relationship between the observable rate constant, k(T), and the reduction temperature, T, can be illustrated by the Arrhenius equation (Equation 28):

$$k(T) = A\exp\left(-\frac{E_a}{RT}\right) \tag{28}$$

and

$$\ln k(T) = \ln A - \frac{E_a}{R}\frac{1}{T}. \tag{29}$$

3 Results

The outcomes from the bulk reduction experiments are discussed, with the reduction degree defined in the Equation 30.

$$Reduction\ degree\ (\%) = \frac{m_1 - m_t}{m_O} \times 100, \qquad (30)$$

where m_1 denotes the weight of the sample prior to reduction, m_t represents the weight of the sample at reduction time t, and m_o signifies the weight of oxygen in the form of iron oxide available for reaction throughout the reduction process.

In the surface reduction experiments, Fe 2p and Fe 3p spectra were quantified and converted to Fe^0, Fe^{2+}, and Fe^{3+} percentages. Based on that, the metallization degree, which refers to the percentage of metallic iron present in the total iron content, has been calculated.

3.1 The surface reduction of iron ore pellets

The APXPS device was employed to investigate the surface (up to 10 nm) reduction of DRI and BF pellets. The results indicate that pellets exhibit varying behavior during surface reduction, influenced by the gas composition, gas flow rate, and pressure, which affect the reduction of both pellets.

Figures 7a and 7b illustrate the Fe 2p and Fe 3p spectra for the DRI sample. The Fe 2p spectra, acquired under ultra-high vacuum and normal temperature circumstances, exhibit seven distinct peaks, including a singular satellite at 719.1 eV. The blue peaks denote Fe^{2+} states, whereas the red peaks signify Fe^{3+} states. Figure 7b illustrates the Fe 3p area, featuring the Fe^{3+} peak at 55.4 eV and the Fe^{2+} peak at 53.8 eV. The presence of both Fe^{2+} and Fe^{3+} chemical states corroborates the identification of magnetite as the specific iron oxide present. The detection of a satellite peak at 719 eV in hematite iron oxide indicates the presence of both hematite and magnetite in the DRI pellets. A satellite peak refers to an additional peak that appears in the photoelectron spectrum alongside the main core-level peak. Prior to reduction with H_2 in the ambient pressure cell, the DRI pellets were subjected to heating in UHV at 700 °C. During the heating in UHV, a reduction in the intensity of the satellite peak at 719 eV was detected, concurrently with an increase in the intensity of Fe^{2+}. Subsequent to vacuum annealing, the sample was positioned within the ambient pressure cell, subjected to a flow of 0.5 sccm (Standard Cubic Centimeters per Minute) of hydrogen for a duration of 60 minutes. Upon the introduction of a 0.5 sccm flow, the intensity of the Fe^{2+} peak augmented;

however, the intensities of the Fe 2p and 3p regions stabilized for 60 minutes at a hydrogen flow rate of 0.5 sccm, signifying the attainment of a steady-state reaction condition. It is crucial to note that the presence of several iron oxides in DRI pellets complicates the differentiation between wüstite and magnetite. It is presumed that prolonged exposure to H_2 results in an enhancement of the peak intensity corresponding to Fe^{2+}, signifying the reduction of magnetite to FeO. The hydrogen flow rate was elevated to 1.15 sccm to further investigate the reduction process. Subsequent to this alteration, a new peak (depicted in orange in Figure 7) appeared at 706.5 electron volts (eV), corresponding to metallic iron (Fe^0) (Yamashita & Hayes, 2008). This indicates the further reduction of magnetite and wüstite to Fe^0. Nevertheless, following prolonged exposure to a hydrogen flow rate of 1.15 sccm, no additional substantial drop of Fe^0 was noted. To optimize the reduction process, the hydrogen flow rate was elevated to 5 sccm for a duration of two hours. This led to a swift escalation in the strength of the Fe^0 peak, signifying an enhanced level of reduction on the pellet surface. Based on the Fe^0 peak intensity during a 2-hour duration with a 5 sccm flow rate, it can be deduced that approximately 93% of the DRI surface was reduced to metallic iron (Fe^0) under these experimental parameters.

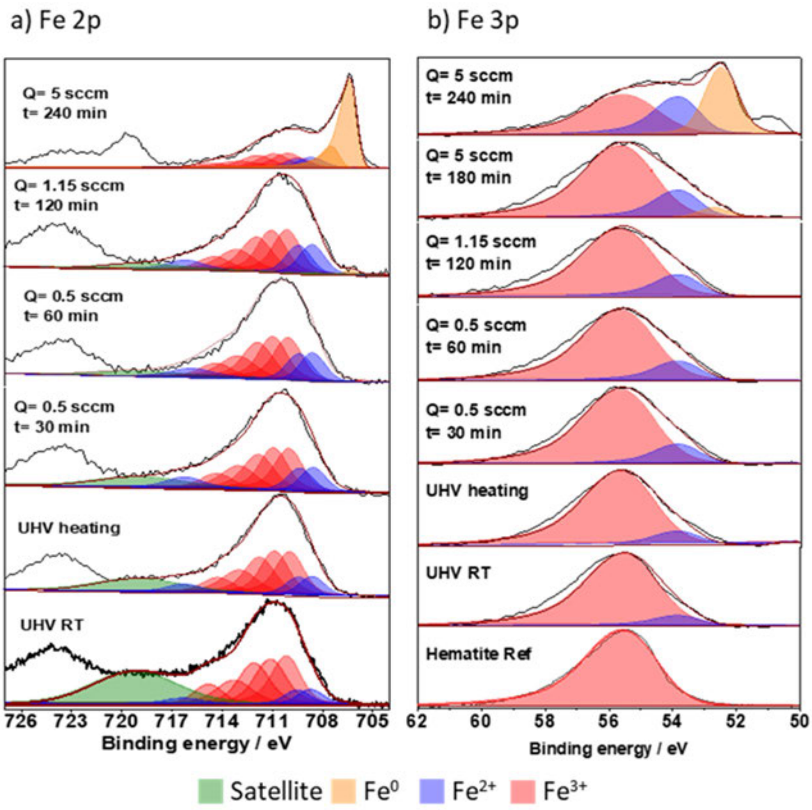

Fig. 7. The APXPS spectrum of a) Fe 2p, and b) Fe 3p from BF pellets during reduction with H_2. Fe 2p and Fe 3p spectra recorded using 900 eV photon energy (Reprinted under CC BY 4.0 license from Publication II © 2024 Authors).

To examine the effect of the reducing gas (CO or H_2), an additional DRI pellet with the same composition was analyzed. The outcomes are illustrated in Figure 8. The DRI pellet was subjected to a CO:H_2 combination (20:80) for 150 minutes at 650 °C with a flow rate of 5 sccm. The cell's total pressure was sustained at 1 mbar. The Fe 2p and Fe 3p spectra (recorded in UHV at room temperature) closely resemble those presented in Figure 7 (Fe 2p and Fe 3p UHV RT), corroborating that the composition of this sample reflects that of the prior DRI sample. Following a 150-minute exposure of DRI pallets to a 5 sccm flow of a CO and H_2 mixture, the Fe 2p spectra closely resemble those obtained in UHV at room temperature. A marginal enhancement in the strength of the Fe^{2+} peaks was noted, signifying the partial reduction of hematite to magnetite; however, no additional reduction to Fe^0 was detected.

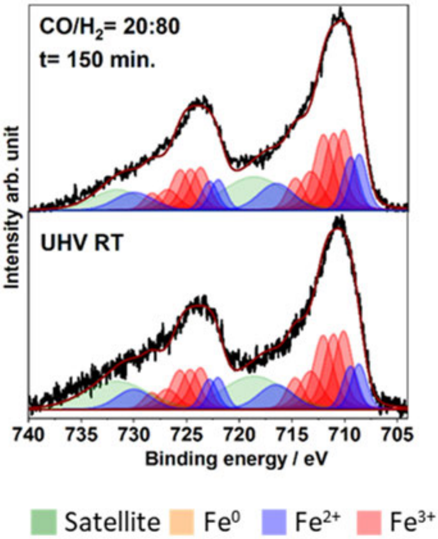

Fig. 8. Fe 2p peak evolution of DRI pellet reduction using a mixture of CO/H_2 as a function of time. Fe 2p and Fe 3p spectra recorded using 900 eV photon energy (Reprinted under CC BY 4.0 license from Publication II © 2024 Authors).

The subsequent step of the inquiry concentrated on examining the surface reduction of the BF sample, employing both pure H_2 and an H_2-CO combination at 650 °C. Figure 9 depicts the reduction of BF pellets at 650 °C in a pure H_2 environment. The measurements were conducted at various pressures between 1 and 2.1 mbar during a duration of approximately 3.5 hours. The aim was to comprehend the impact of varying pressure in a pure H_2 atmosphere at 650 °C on the reduction process. The Fe 2p spectra, obtained under ultra-high vacuum settings, closely resemble those of hematite (Fe_2O_3, Fe^{3+}) reference samples, thereby demonstrating that the BF pellets were composed solely of hematite. During H_2 dosing at 1 mbar pressure and 650 °C, the BF pellets swiftly transitioned from hematite (Fe^{3+}) to a probable mixture of magnetite and wüstite (Fe^{2+}), as seen by the heightened strength of the Fe^{2+} peaks. Administering H_2 at a pressure of 1 mbar for a further 30 minutes yielded no notable further decline. As a result, the pressure was elevated to 2.1 mbar, while the temperature remained constant at 650 °C and the flow rate at 5 sccm. The increase in pressure resulted in a further decrease of Fe^{2+} to Fe^0 within 60 minutes, as evidenced by the emergence of the Fe^0 state at 706.5 eV. The strength of the Fe^0 peak augmented over time, signifying the conversion of Fe^{2+} to Fe^0. After 210 minutes, the reduction process attained a steady state, as evidenced by the stable Fe^0 peak intensity.

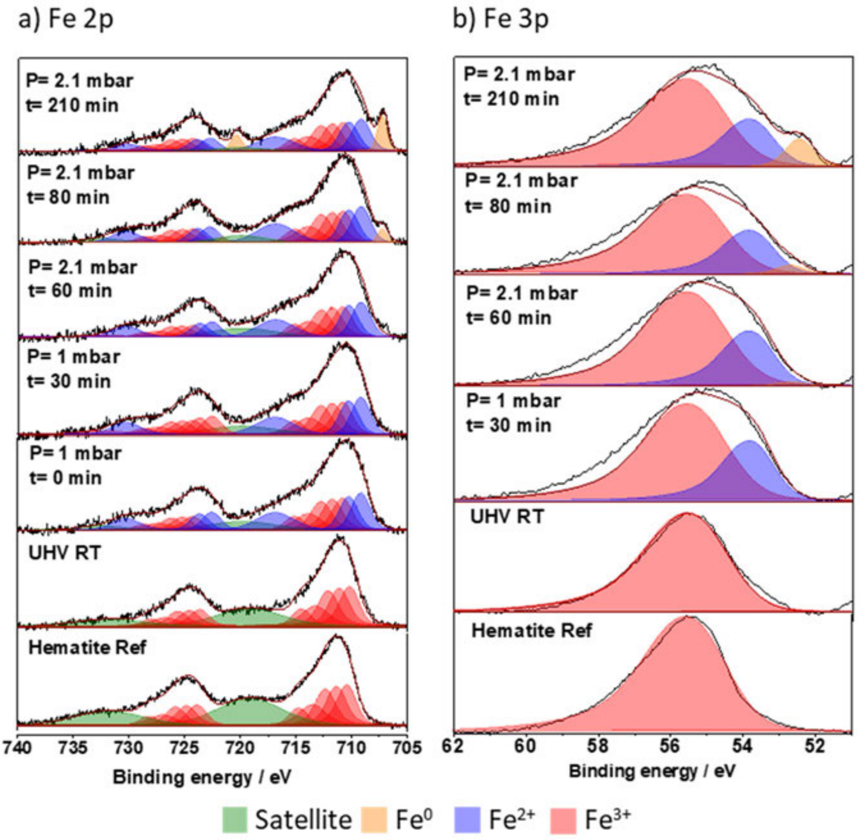

Fig. 9. The APXPS spectrum of a) Fe 2p, and b) Fe 3p from BF pellets during reduction with H_2. Fe 2p and Fe 3p spectra recorded using 900 eV photon energy (Reprinted under CC BY 4.0 license from Publication II © 2024 Authors).

A new BF pellet was subsequently put into the reaction chamber and reduced in a CO and H_2 mixture at 650 °C. Figure 10 displays the Fe 2p and 3p spectra, obtained in the presence of a CO and H_2 combination. All in situ spectra were recorded at a flow rate of 10 sccm, with the overall pressure in the reaction chamber held at 2 mbar. The Fe 2p and 3p spectra were initially recorded in pure CO with a flow rate of 10 sccm for 60 minutes. Hematite was noted to be converted to Fe^{2+} with a 10 sccm flow of pure CO. Nonetheless, no additional reduction was detected in pure

CO. Consequently, after 60 minutes, the composition was modified to incorporate 30% H_2 for an additional 30 minutes, although no further reduction was seen. As a result, the H_2 flow was augmented to achieve a gas mixture including 50% H_2. The initial finding was a substantial reduction of Fe oxides to Fe^0 following this rise. Additional reduction was observed under stable settings for a duration of up to 290 minutes. After 240 minutes, a drop in the strength of the Fe^0 peak (in the Fe 2p region at 707 eV and in the Fe 3p region at 52 eV) was noted, accompanied by a rise in the intensity of the Fe^{3+} peak, signifying the reoxidation of Fe^0 to Fe^{3+}. Figure 11 illustrates the temporal evolution of the Fe 2p peak corresponding to the differing percentages of CO and H_2 mixtures.

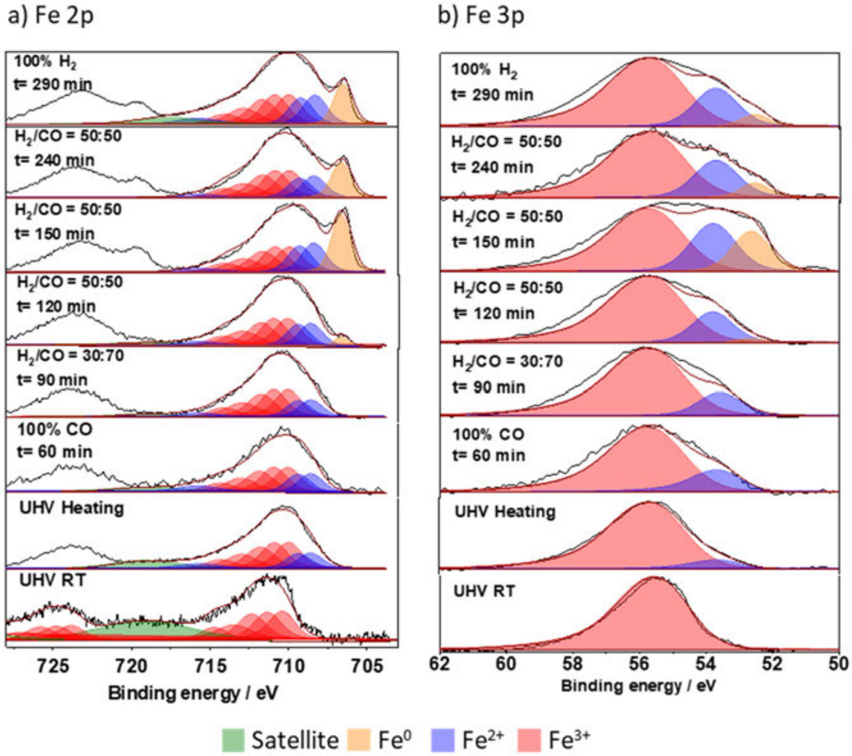

Fig. 10. The APXPS spectrum of a) Fe 2p and b) Fe 3p from BF pellet during reduction with mixture of CO and H_2. The spectra were recorded in 10 sccm constant flow at 650 °C. Fe 2p and Fe 3p spectra recorded using 900 eV photon energy (Reprinted under CC BY 4.0 license from Publication II © 2024 Authors).

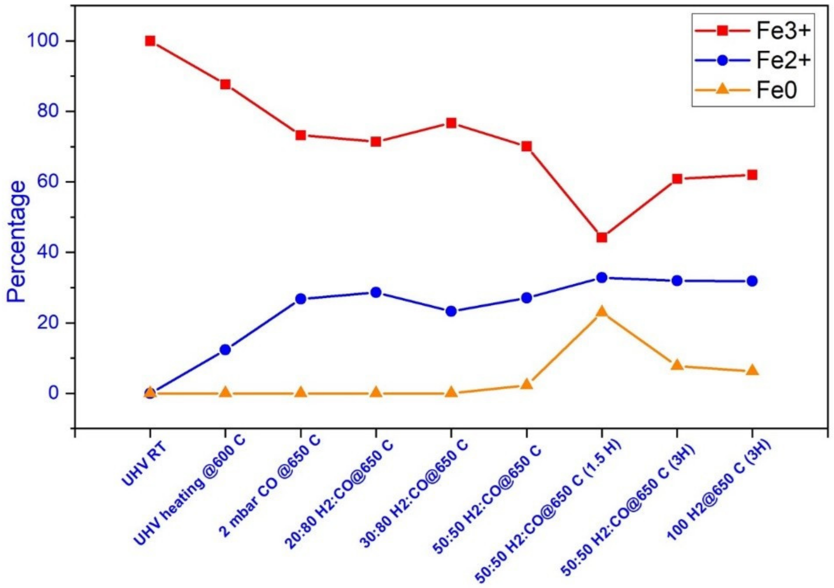

Fig. 11. The evolution of Fe 2p peaks for BF pellet at 650 °C as a function of time under varying compositions of CO and H_2 mixtures (Reprinted under CC BY 4.0 license from Publication II © 2024 Authors).

3.2 The bulk reduction of iron ore pellets

The single pellet reduction of a blast furnace (BF) pellet and a direct reduced iron (DRI) pellet were conducted utilizing thermogravimetric analysis (TGA). The pellets were reduced in pure CO and pure H_2 environments with a constant flow rate of 2 l/min at temperatures ranging from 700 °C to 1100 °C.

Figure 12 illustrates the reduction curves derived from the TGA reduction tests conducted at various temperatures. The requisite reduction degree for theoretical complete conversion to magnetite is 10.1% for DRI pellets and 10.9% for BF pellets. The reduction degree for full conversion to wüstite (FeO) is 32.6% for DRI pellets and 33.2% for BF pellets. The values, obtained from the chemical composition of the pellets, are depicted by dashed lines in Figure 12. Both pellets underwent a maximum reduction degree approaching 100% during hydrogen reduction. When carbon monoxide served as the reducing agent, the BF pellet attained a reduction degree of 32% at 700 °C and 67% at 800 °C, but the DRI pellet achieved 28% and 59% at the corresponding temperatures. At 1000 °C and 1100 °C, the DRI pellet attained reductions of 93% and 100%, while the BF pellet obtained reductions of 88% and 94%, respectively. In both instances of reduction with H_2 and CO, and for both pellets, elevating the temperature resulted in an enhanced reduction rate and the attainment of a greater degree of reduction. Figure 12 illustrates that during the hydrogen reduction of both DRI and BF pellets, temperature exerted a more pronounced influence throughout the range of 700–900 °C. A rise in temperature from 1000 to 1100 °C resulted in only a marginal increase in the decrease rate.

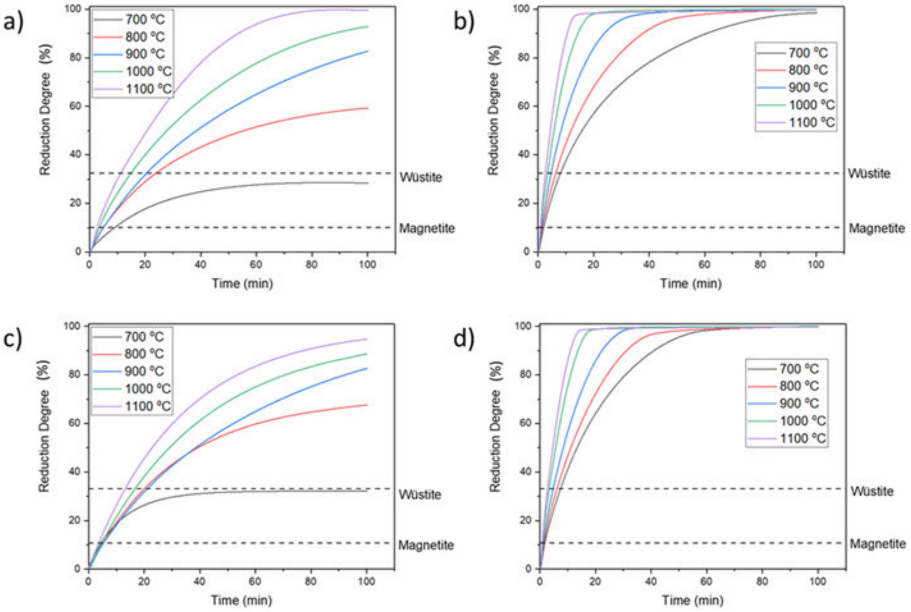

Fig. 12. Reduction curves for a) a DRI pellet with CO, b) a DRI pellet with H_2, c) a BF pellet with CO, and d) a BF pellet with H_2 at different temperatures (Reprinted under CC BY 4.0 license from Publication III © 2024 Authors).

To gain a deeper insight into the chemical reactions, we carried out X-ray diffraction (XRD) investigations to complement the reduction experiments. Figure 13 illustrates the XRD results of both unreduced and reduced DRI and BF pellets subjected to H_2 and CO at different temperatures. At 700 °C, the hydrogen-reduced DRI pellet displays subtle peaks of wüstite alongside prominent peaks of metallic iron. This indicates that a small amount of wüstite persisted in its unreduced state, affirming that the conversion of wüstite to metallic iron is the most sluggish and pivotal phase in the reduction process. At increased temperatures, only metallic iron is observed, signifying the successful completion of the reduction process to iron.

In the context of reduction by CO at 700 ℃, the DRI pellet has minor magnetite peaks, indicating a tiny quantity of residual unreduced magnetite, alongside prominent peaks of wüstite, suggesting that wüstite is the dominating phase. Nonetheless, only the wüstite phase is observable when the BF pellet is reduced at 700 ℃. At 800 ℃, the XRD results for the BF pellet reveal wüstite and minor peaks of metallic iron, which are also present in the DRI pellet; however, the peaks of wüstite in the DRI pellet are significantly more pronounced, suggesting a greater abundance of wüstite in that sample. The XRD results of both pellets at 900 ℃ are analogous, with wüstite as the predominant phase alongside metallic iron. At 1000 ℃, the predominant phase for both pellets is metallic iron, while the secondary phase is wüstite; nevertheless, the metallic iron peaks in the DRI pellet are more pronounced. At 1100 ℃, the XRD results of the DRI pellet reveal only metallic iron, whereas wüstite peaks persist in the XRD results of the BF pellet.

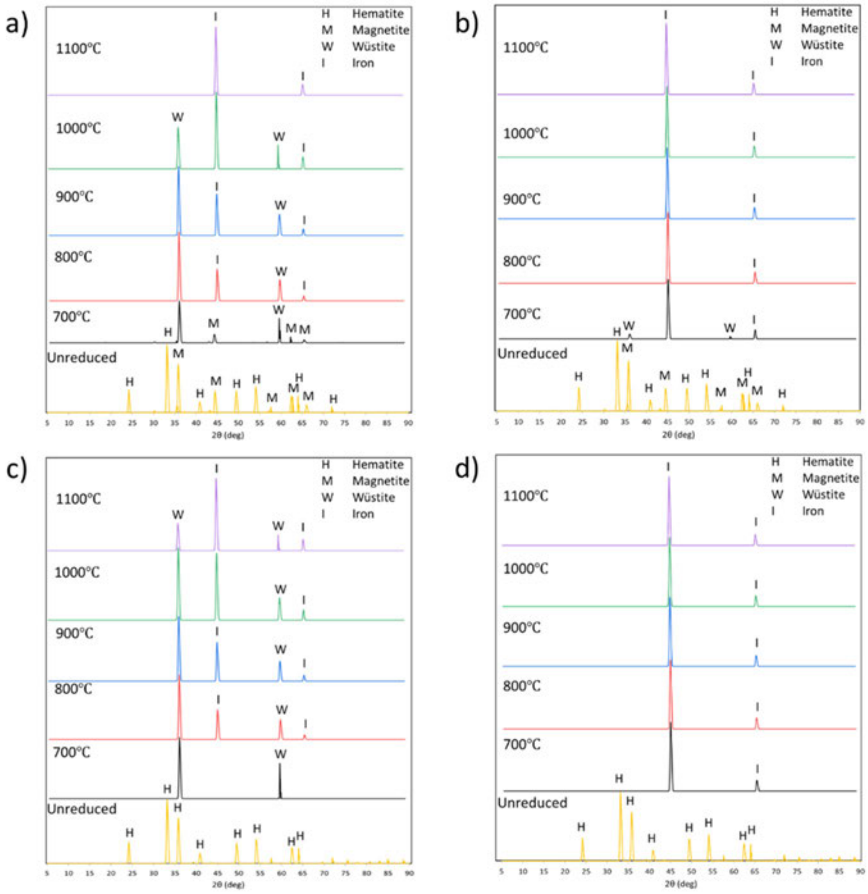

Fig. 13. XRD results for the reduction of a) a DRI pellet with CO, b) a DRI pellet with H_2, c) a BF pellet with CO, and d) a BF pellet with H_2 at different temperatures (Reprinted under CC BY 4.0 license from Publication III © 2024 Authors).

Figure 14 shows the FESEM images of CO-reduced pellets at different temperatures. At 700 °C, metallic iron is not observable. Nonetheless, SiO_2 and other gangue oxides appear as a singular grain, separate from iron oxides, or situated at the boundary of iron oxide grains.

At 800 °C, despite the presence of significant interconnected porosities and cracks in the DRI pellet's structure, only a thin layer of metallic iron forms at the grain rims, inhibiting further reduction. In contrast, the BF pellet, characterized by its denser composition, demonstrates a more sophisticated reduction process and a thicker layer of metallic iron (Figure 14b).

At 900 °C, reduction advances from the grain borders to the grain cores in both pellets, making them practically indistinguishable. The emergence of porosities and cracks is observable from 700 °C, but an elevation to 900 °C leads to a significant rise in porosity development, facilitating reduction. Nevertheless, some wüstite is discernible in the structure of the BF pellet, especially inside the larger grains.

At 1100 °C, a similar situation occurs, in which the DRI pellet experiences total reduction, whereas wüstite is still identifiable in specific areas of the BF pellet's structure.

Figure 15 displays FESEM images of DRI and BF pellets subjected to reduction with hydrogen. At 700 °C, only trace amounts of wüstite are observed in certain areas of the DRI pellet, consistent with the findings of other researchers (Zakeri et al., 2025). Unlike the reduction with CO, which failed to infiltrate the thick structure of the BF pellet and reduce the grain core, the use of hydrogen as a reducing agent resulted in complete reduction even at lower temperatures. This indicates that hydrogen possesses enhanced reduction capabilities and diffuses more efficiently. Notably, in regions where iron oxides were encapsulated in gangue oxides (predominantly SiO_2), hydrogen successfully diffused and reduced the iron oxide (Figure 15e).

Analogous to the reduction process involving CO, elevated temperatures, particularly beyond 900 °C, resulted in the expansion and formation of porosities and cracks during hydrogen reduction. The proliferation of porosities and cracks was more significant during carbon monoxide reduction than during hydrogen reduction, which has been observed also by Szekely et al. (Szekely & El-Tawil, 1976). This disparity becomes further apparent at temperatures of 1000 and 1100 °C.

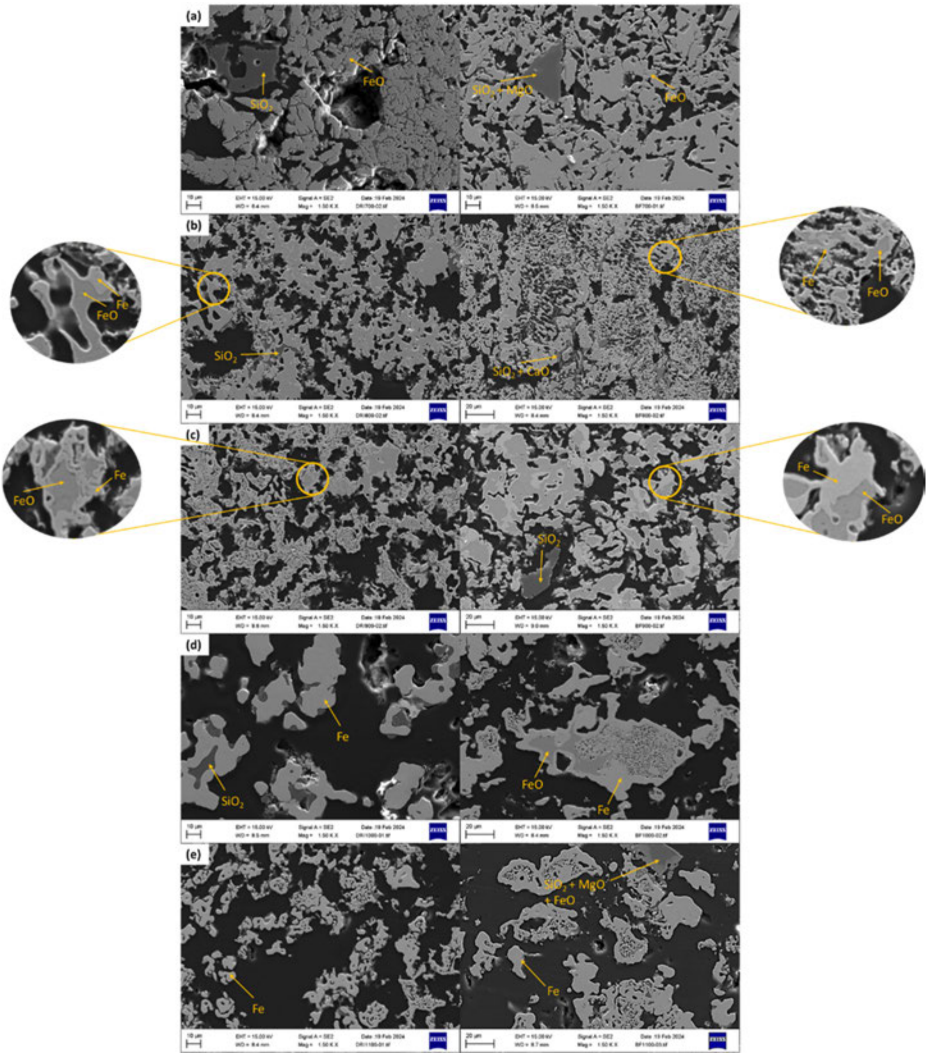

Fig. 14. FESEM images for CO reduced DRI pellets on the left and BF pellets on the right at a) 700, b) 800, c) 900, d) 1000, e) 1100 ˚C (Reprinted under CC BY 4.0 license from Publication III © 2024 Authors).

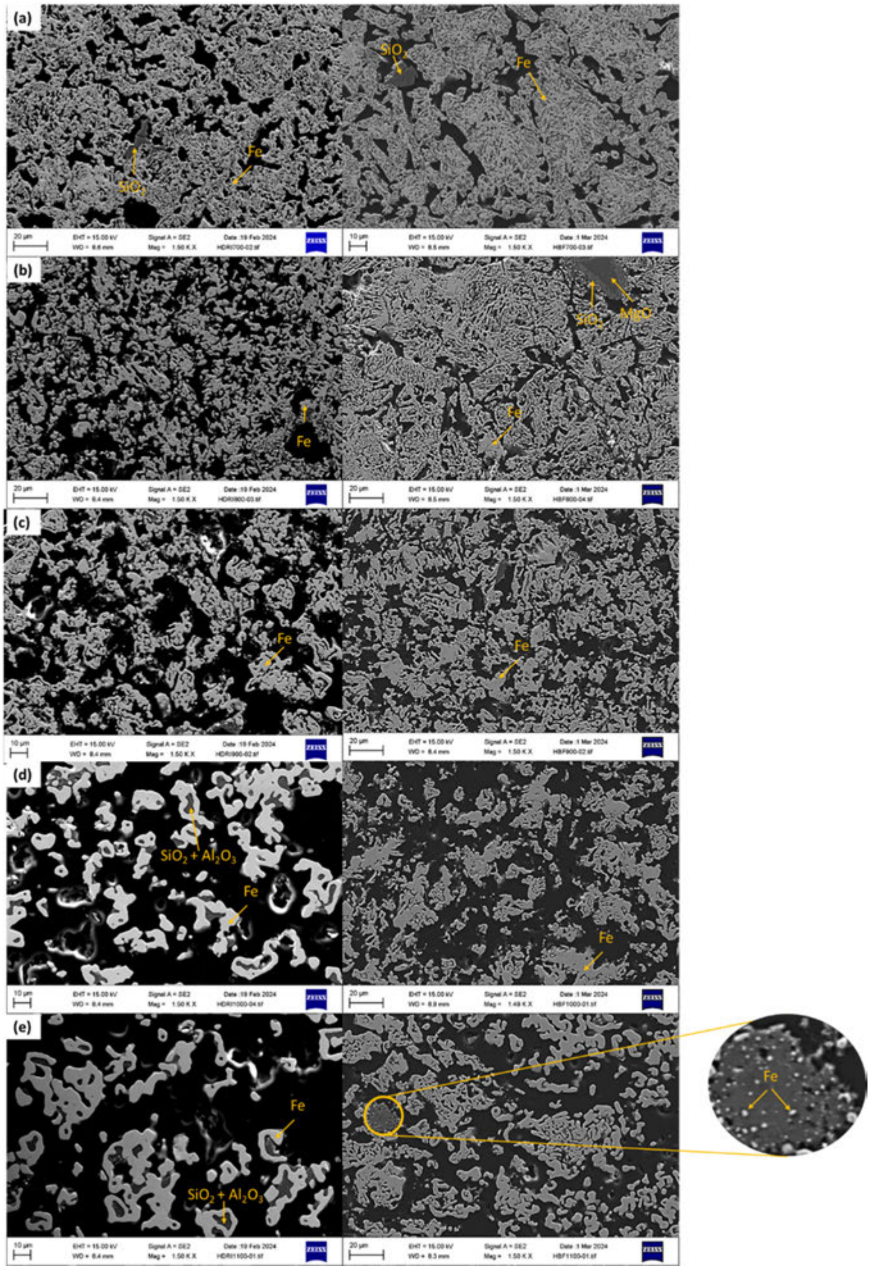

Fig. 15. FESEM images for H_2 reduced DRI pellets on the left and BF pellets on the right at a) 700, b) 800, c) 900, d) 1000, e) 1100 ℃ (Reprinted under CC BY 4.0 license from Publication III © 2024 Authors).

3.3 The effect of water vapor on the hydrogen reduction of iron ore pellets

The impact of added water vapor on the hydrogen reduction of iron ore pellets, which are used in direct reduction process was examined. Isothermal single-pellet reduction tests were performed using TGA in gas atmospheres with different ratios of water vapor and hydrogen (30% H_2O + 70% H_2, 20% H_2O + 80% H_2, 10% H_2O + 90% H_2, and 100% H_2) within a temperature range of 800 ℃ to 1000 ℃.

Figure 16 demonstrates that the gas compositions and temperatures were chosen to render the complete reduction to metallic iron thermodynamically feasible.All isothermal studies conducted at a constant gas flow rate of 2000 ml/min, samples were cooled down to 20 ℃ in a nitrogen environment after a reduction period of 110 minutes.

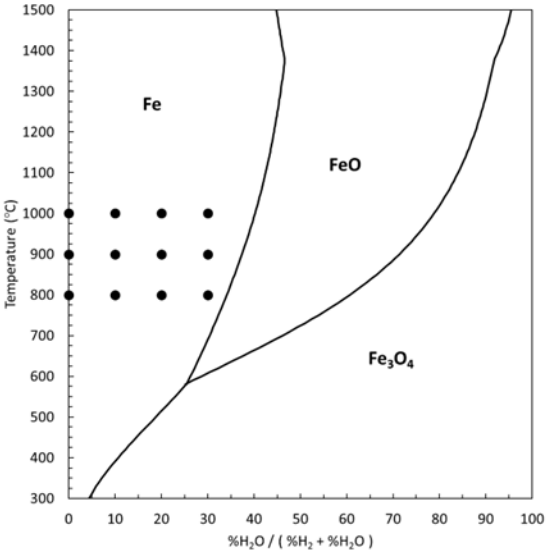

Fig. 16. Baur–Glaessner diagram. Each point represents one isothermal experiment (calculated with HSC Chemistry version 10.4.1.1) (Reprinted under CC BY 4.0 license from Publication III © 2024 Authors).

Figure 17 depicts the results of isothermal reduction experiments performed at temperatures between 800 ℃ and 1000 ℃, with water vapor concentrations ranging from 0% to 30%. It is clear that when the temperature rises, the rate of reduction correspondingly escalates. This effect, however, fluctuates based on the gas composition and the reduction stage. For example, utilizing pure hydrogen, the time required to reach the maximum reduction degree decreases from 79 minutes at 800 ℃ to 50 minutes at 900 ℃ and 29 minutes at 1000 ℃, respectively. The influence of temperature on the reduction rate is amplified with 10% water vapor, resulting in a further decrease in the time needed to achieve maximum reduction degree.

A comparison of Figures 17a and 17b reveals that an increase in the water vapor content diminishes the reduction rate and extends the reduction time, with the gas composition having a more significant impact at lower temperatures. Figure 17c illustrates the significant influence of temperature on the rate of reduction in the presence of 20% water vapor. The maximum reduction degree is attained after 61 minutes at 1000 ℃, whereas the reduction process fails to achieve equilibrium within 110 minutes at both 900 ℃ and 800 ℃, progressing at a diminished rate. Figure 17d indicates that while reduction may seem to cease after the second step, temperature continues to significantly influence the reduction rate.

Moreover, Figure 17 illustrates that the initial reduction step (hematite to magnetite) occurs rapidly and is independent of the temperature and water vapor concentration. Both the temperature and water vapor content affect the rate of the second stage (magnetite to wüstite), with the influence of water vapor content becoming more significant beyond 10%. Furthermore, elevated water vapor levels amplify the effect of temperature on the reduction rate. Figures 17a, 17b, and 17c demonstrate that temperature exerts its most substantial influence on the reduction rate in the last phase (wüstite to iron).

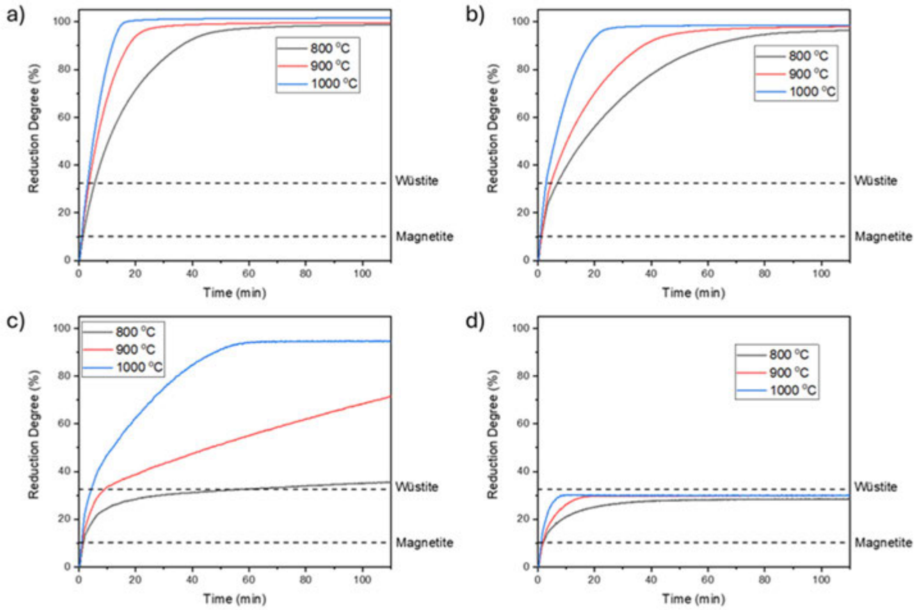

Fig. 17. Hydrogen reduction curves with a) 100% H_2, b) 90% H_2 + 10% H_2O, c) 80% H_2 + 20% H_2O, d) 70% H_2 + 30% H_2O at different temperatures (Reprinted under CC BY 4.0 license from Publication IV © 2025 Authors).

Figure 18 illustrates the maximum degree of reduction under various reaction conditions. Significantly, complete reduction occurs at all temperatures. The introduction of 10% water vapor has a minimal impact on the reduction degree, closely mirroring results achieved with pure hydrogen. Nonetheless, with 20% water vapor, a significant drop in the degree of loss is seen, especially between 800 °C and 900 °C. The decrease in the reduction degree is less significant at 1000 °C. With 30% water vapor, the maximum reduction degree consistently hovers around 30% across all temperatures, suggesting that the reduction of wüstite to metallic iron does not commence, despite its thermodynamic viability. Furthermore, Figure 18 highlights that the effect of temperature on the degree of reduction is substantial solely with 20% water vapor in the gas mixture.

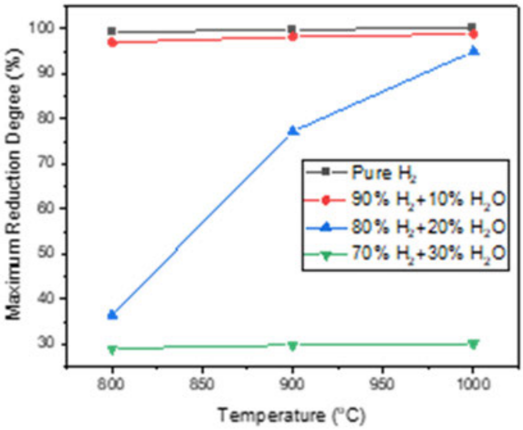

Fig. 18. Maximum reduction degree at different temperatures and with different gas compositions (Reprinted under CC BY 4.0 license from Publication IV © 2025 Authors).

Figures 19a, 19b, and 19c illustrate the FESEM pictures of pellets reduced with pure hydrogen at different temperatures. At 800 °C, while metallic iron is predominant, areas of unreduced wüstite are seen within the cores of some larger grains. In contrast, at 900 °C and 1000 °C, the microstructure of reduced pellets exhibits metallic iron as the exclusive phase, alongside darker gray gangue elements.

Figures 19d, 19e, and 19f illustrate the FESEM results of pellets reduced using a composition of 90% H_2 and 10% H_2O. At 800 °C, some grains exhibit the existence of unreduced wüstite, with its content significantly higher than that in pellets reduced exclusively with hydrogen. At 900 °C, metallic iron is the predominant phase, while occasional residues of wüstite are seen within the cores of larger grains. At 1000 °C, wüstite is no longer detectable, indicating nearly total reduction of the particle.

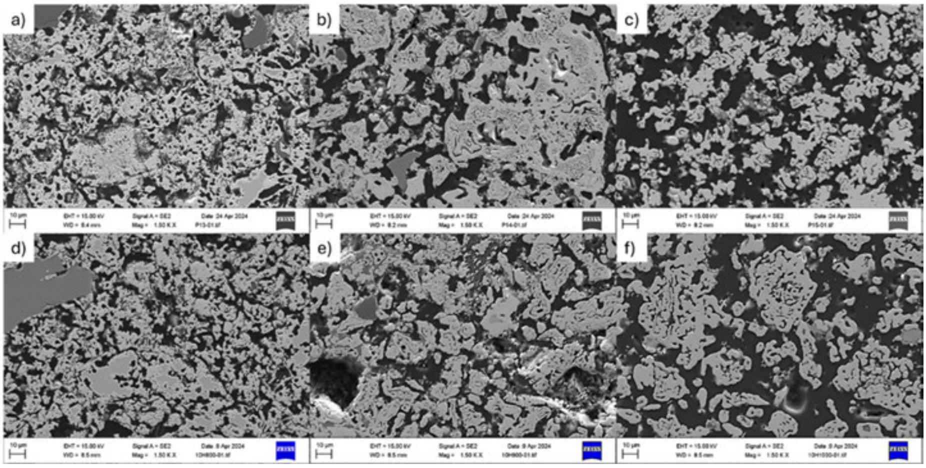

Fig. 19. FESEM images of reduced pellets with 100% H_2 at a) 800 ˚C, b) 900 ˚C, d) 1000 ˚C, and reduced pellets with 90% H_2+10% H_2O at d) 800 ˚C, e) 900 ˚C, f) 1000 ˚C (Reprinted under CC BY 4.0 license from Publication IV © 2025 Authors).

Figure 20a depicts the dense microstructure of reduced pellets produced with a gas mixture of 80% H_2 and 20% H_2O, mostly consisting of wüstite and gangue oxides, with no observable metallic iron. In contrast, Figure 20b illustrates that at 900 ℃, the formation of metallic iron commences at the grain boundaries and progresses into the core, whereas wüstite continues to be the predominant phase in larger grains. At an elevated temperature of 1000 ℃ (Figure 20c), metallic iron emerges as the dominating phase, while wüstite is primarily found in larger grains.

In contrast, Figures 20d, 20e, and 20f demonstrate that the microstructure of pellets reduced with 30% water vapor in the reducing gas shows no presence of metallic iron at any temperature. Wüstite serves as the primary component, with minor traces of other phases, predominantly SiO_2, detected in the thick microstructure of the pellets.

Moreover, Figures 19 and 20 illustrate that regardless of the water vapor level in the reducing gas, increasing the temperature promotes the development and enlargement of pores and microcracks. Increasing the water vapor content in the reducing gas significantly diminishes the porosity of the reduced pellets, resulting in a denser microstructure, particularly when the water vapor percentage surpasses 10%. However, elevated reduction temperatures can alleviate this effect.

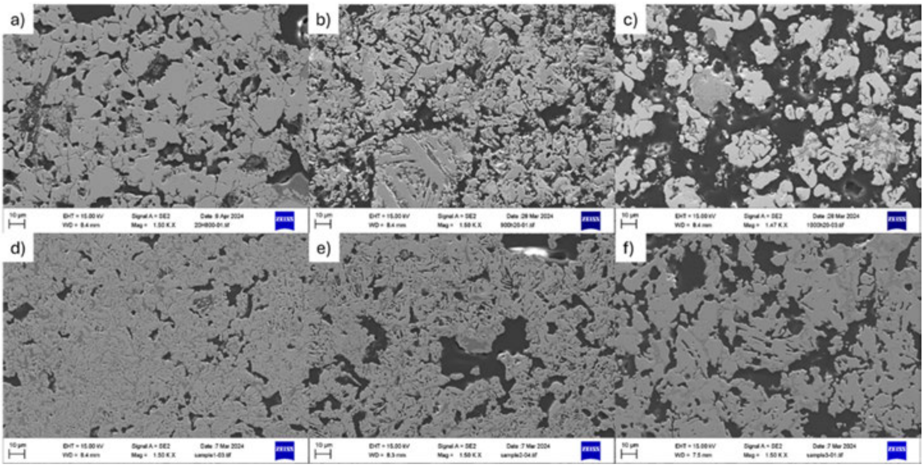

Fig. 20. FESEM images of reduced pellets with 80% H_2+20% H_2O at a) 800 ˚C, b) 900 ˚C, d)1000 ˚C, and reduced pellets with 70% H_2+30% H_2O at d) 800 ˚C, e) 900 ˚C, f) 1000 ˚C (Reprinted under CC BY 4.0 license from Publication IV © 2025 Authors).

4 Discussion

4.1 Comparison between DRI and BF pellets

Because of the differences in the initial chemical composition and physical properties of BF and DRI pellets, they showed different behaviours during reduction in terms of both the surface and bulk scale. The reduction, microstructure, and kinetics of the pellets will be compared and discussed in the following sections.

4.1.1 Reduction and microstructure

Figure 21a shows the contour plot of Fe^{3+}, Fe^{2+}, and Fe^{0} on the surface of DRI pellets based on the Fe 3p and Fe 2p spectra, during the reduction by hydrogen. It can be observed that the reduction of hematite to magnetite started from the beginning even with the low H_2 flow rate of 0.5 sccm. The reduction did not progress further with 0.5 sccm. By increasing the flow rate to 1.15 sccm, wüstite was formed. Increasing the flow rate to 5 sccm led to the reduction of the DRI sample to around a 90% metallization degree in 2 hours. Increasing the flow rate elevates the reaction rate by raising the hydrogen concentration at the reaction interface. Additionally, resistance to gaseous diffusion around the pellet decreases by increasing the gas flow especially at low temperatures. It has been reported previously that there is a critical gas velocity, which depends on the temperature, and below which the gas flow rate controls the rate of reaction (Kawasaki et al., 1962; Kuila et al., 2016b). Kang et al. found that increasing the hydrogen flow rate promotes the reaction rate by decreasing the activation energy and effect is more significant for reduction of magnetite to wüstite and wüstite to metallic iron steps (Kang et al., 2023).

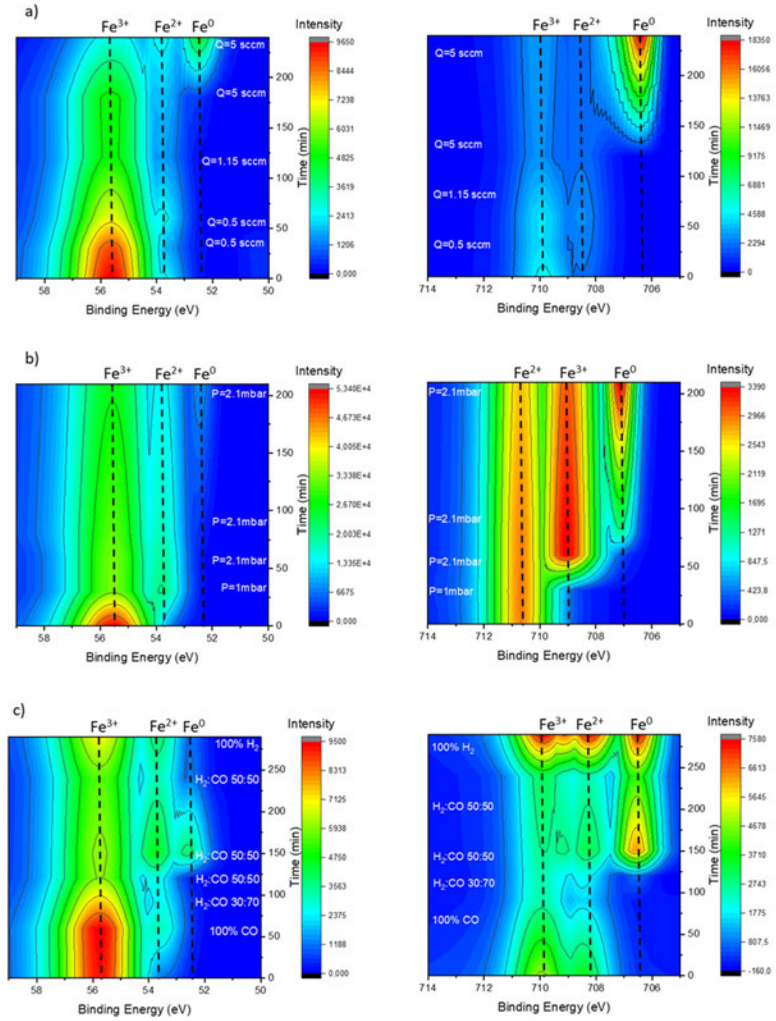

Fig. 21. The contour plot for Fe^{3+}, Fe^{2+}, and Fe^{0} intensities during the reduction of a) a DRI pellet by H_2 with different flow rates, b) a BF pellet by H_2 at a different pressure, and c) BF pellet by mixture of CO-H2 with different ratio based on Fe 3p (left) and Fe 2p (right) spectra (Reprinted under CC BY 4.0 license from Publication II © 2024 Authors).

The contour plot of different iron ions at the surface during the hydrogen reduction of BF pellet in different conditions is illustrated in Figure 21b. Increasing the Fe^{2+} concentration together with a decrease in Fe^{3+} indicates a high-rate reduction of hematite to magnetite by H_2 at 1 mbar and then it became slower. After 30 minutes no changes were observed. By increasing the H_2 pressure from 1 mbar to 2.1 mbar, wüstite started to form but at a lower rate. Furthermore, after 80 minutes wüstite started to reduce to metallic iron. Since the gas flow rate is constant (5 sccm), increasing the pressure leads to a longer residence time of the gas and consequently increases the reduction rate. Habermann et al. showed that by increasing the pressure at a constant flow rate, the rate of reduction significantly increases at the final stage of reduction (fractional reduction higher than 0.5), which represents the reduction of wüstite to metallic iron (Habermann et al., 2000). This phenomenon is compatible with the results in Figure 9b. As Fe^0 rises and Fe^{2+} falls, it suggests a faster reduction rate from wüstite to metallic iron compared to magnetite to wüstite at an elevated pressure. However, even at a higher pressure the metallization degree achieved from the hydrogen reduction of the BF pellets is approximately 9%, which is significantly lower than the 90% observed for the DRI pellets.

Using higher reduction temperatures (700 to 1100 °C) and a higher gas flow rate (2 l/min) no diffusion barrier was detected during the bulk reduction of both pellets and they both showed similar behaviour and reached almost complete reduction. However, the DRI pellet showed a higher reduction rate, which is because of its higher porosity in comparison to the BF pellet. Moreover, some traces of wüstite were detected in the reduced DRI pellet at 700 °C, especially in the center of the coarser grains.

By adding 20% CO to the gas mixture to reduce the surface of DRI pellet, only a slight reduction to magnetite was observed and the reduction did not proceed further even with 5 sccm flow rate. High level of magnetite (9.11%) in the chemical composition of DRI pellet may explain this phenomenon. The reduction of magnetite is more difficult than that of hematite due to the hard and dense shell of magnetite (Edstrom, 1953; Heikkilä et al., 2020). Because of the larger molecular size of CO in comparison to H_2 and the lower reducing ability, adding 20% CO to the gas mixture decreases the mobility and diffusibility of the reducing gas and consequently cannot reduce the DRI sample with high amount of magnetite.

The surface reduction of the BF pellets by different gas mixtures can be observed in Figure 21c. Increasing the Fe^{2+} and decreasing the Fe^{3+} shows that the reduction of hematite to magnetite started from the beginning using CO as the reducing gas. Progress was observed by adding 30% H_2 and the magnetite started to reduce to wüstite. Increasing the percentage of H_2 to 50%, led to the formation of metallic iron and after 150 minutes a 20% metallization degree was detected. An increase in the percentage of Fe^{2+} indicates that the reduction of magnetite to wüstite was ongoing at the same time. Interestingly, by continuing the reduction with a mixture of CO and H_2 (50:50), the level of Fe^0 fell dramatically, indicating the reoxidation of the surface, and after 290 minutes, this became stable. The results from the Fe 2p analysis indicate that substituting the gas mixture with 100% H_2 at the 240-minute mark led to a surface reduction to metallic iron. However, the Fe 3p contour plot suggests that the introduction of 100% H_2 did not alter the conditions within the deeper layers of the pellet.

To understand the unexpected reoxidation of the surface, the reduced sample was studied also by FESEM. In Figure 22, DRI pellets exhibit surface pores of varying sizes extending towards the core, aiding gas diffusion and contributing to high metallization in hydrogen reduction. In contrast, the BF sample surface features numerous minute pores where water vapor and carbon dioxide accumulate during reduction due to the low temperature and flow and block the active sites on wüstite (Moukassi et al., 1983; Spreitzer & Schenk, 2019b), especially on the concave interfaces (Nie et al., 2024). Because the pores are not connected to the internal parts of the sample, the pressure of water vapor and carbon dioxide inside them increases locally and causes reoxidation to wüstite and then magnetite. Put simply, the produced water vapor and carbon dioxide remain unremoved, causing a reduction in the hydrogen and carbon monoxide concentration at the reaction interface when the flow rate is not high enough (Kang et al., 2024b). Figure 23 schematically illustrates this phenomenon.

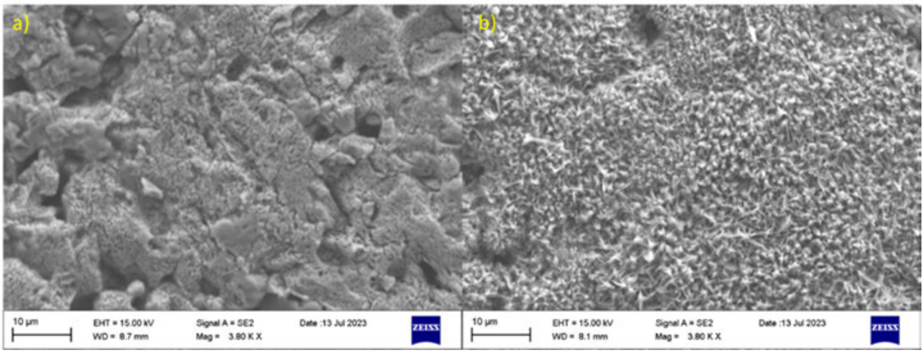

Fig. 22. FESEM image of a) reduced DRI pellets with H_2, b) a reduced BF pellet using mixture of CO-H_2 (50:50) after 3 hours (Reprinted under CC BY 4.0 license from Publication II © 2024 Authors).

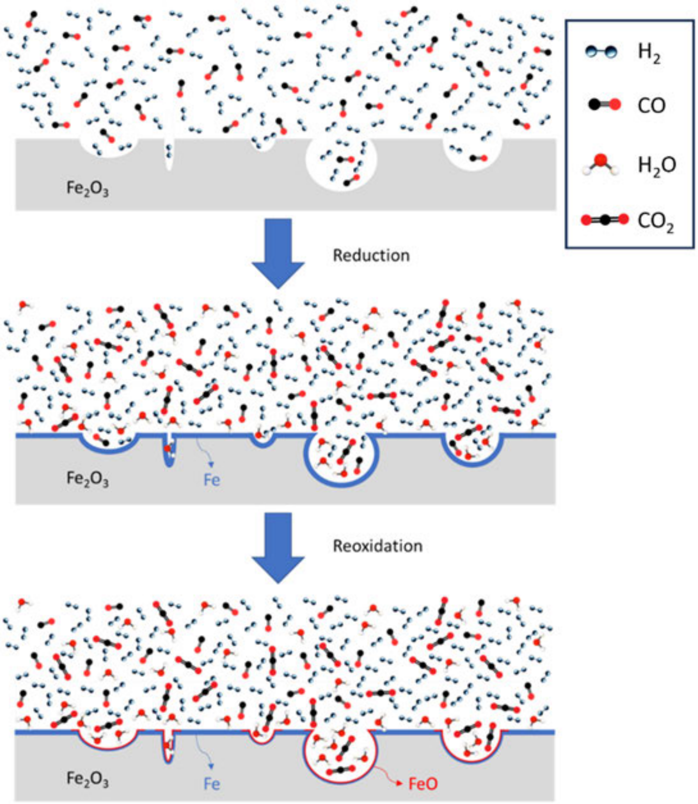

Fig. 23. Schematic of mechanism of reduction and reoxidation of BF pellet in CO-H_2 (50:50) atmosphere. First, the surface of the sample is reduced by H_2 and CO and a layer of metallic iron is formed on the surface. Over time, the partial pressure of CO_2 and H_2O increases, especially in the porosities, and this causes reoxidation (Reprinted under CC BY 4.0 license from Publication II © 2024 Authors).

Figure 24 shows the phase stability diagram of Fe-O-C and Fe-O-H at 650 °C, which represent the reduction of BF with CO and H_2, respectively. The diagrams have been drawn using HSC Chemistry software based on the Gibbs free energy and thermodynamic database. Each line represents a reaction between two substances at the equilibrium condition. Although the partial pressure of CO, CO_2, H_2, and H_2O cannot be determined exactly in our experiments, the estimated pressure range for the components mentioned has been shown by a red circle in the diagrams. It can be observed that by increasing the partial pressure of CO_2 and H_2O produced in the reduction reactions, wüstite becomes stable. Since the stability area of wüstite is very small, a further increase in partial pressures of CO_2 and H_2O leads to the reduction of wüstite to magnetite, which justifies the increasing Fe^{3+} in Figure 21c during the reoxidation. The reoxidation reactions are illustrated as reactions 31–34:

$$Fe\ (s) + CO_2\ (g) \rightleftharpoons FeO\ (s) + CO\ (g), \tag{31}$$

$$3FeO\ (s) + CO_2\ (g) \rightleftharpoons Fe_3O_4\ (s) + CO\ (g), \tag{32}$$

$$Fe\ (s) + H_2O\ (g) \rightleftharpoons FeO\ (s) + H_2\ (g), \tag{33}$$

and

$$3FeO\ (s) + H_2O\ (g) \rightleftharpoons Fe_3O_4\ (s) + H_2\ (g). \tag{34}$$

For the reactions 7–10, the Gibbs free energy can be given by the equations 35–38 respectively:

$$\Delta G = \Delta G^0 + RT \ln \frac{a_{FeO}\, P_{CO}}{a_{Fe}\, P_{CO_2}}, \tag{35}$$

$$\Delta G = \Delta G^0 + RT \ln \frac{a_{Fe_3O_4}\, P_{CO}}{a_{FeO}^3\, P_{CO_2}}, \tag{36}$$

$$\Delta G = \Delta G^0 + RT \ln \frac{a_{FeO}\, P_{H_2}}{a_{Fe}\, P_{H_2O}}, \tag{37}$$

and

$$\Delta G = \Delta G^0 + RT \ln \frac{a_{Fe_3O_4}\, P_{H_2}}{a_{FeO}^3\, P_{H_2O}}, \tag{38}$$

where ΔG is the Gibbs free energy, ΔG^0 is the standard Gibbs free energy, R is the universal gas constant, T is the temperature, a_{Fe}, a_{FeO}, and a_{Fe2O3} are the activity of Fe, FeO, and Fe_3O_4 respectively, and P_{CO} and P_{CO2} are the partial pressure of CO and CO_2 respectively. For pure substances $a_{Fe} = a_{FeO} = a_{Fe2O3} = 1$. Therefore, it is evident that at a fixed temperature, elevating the partial pressures of H_2O and CO_2 decreases the ΔG values, prompting oxidation reactions to occur spontaneously.

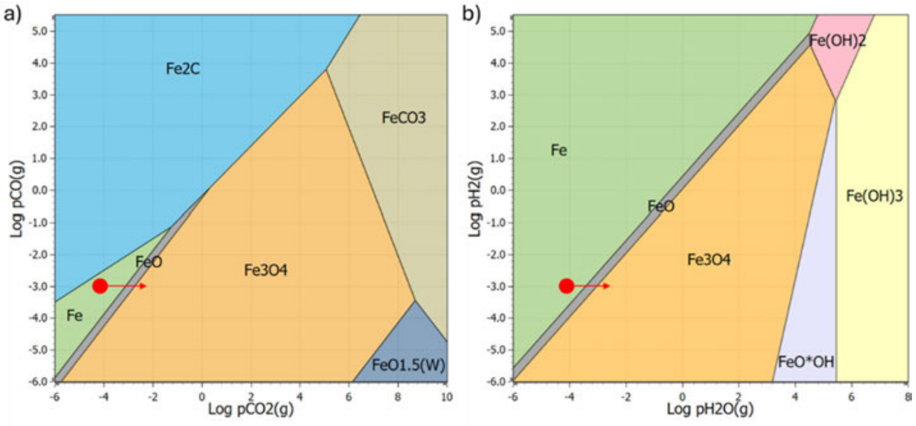

Fig. 24. Phase stability diagrams of a) Fe-O-C, and b) Fe-O-H systems at 650 °C. The red circle shows the initial point for reduction with CO-H_2 (50:50). The arrow shows that as the reduction proceeds, the partial pressure of CO_2 and H_2O increases, which causes the reoxidation to wüstite and magnetite (Reprinted under CC BY 4.0 license from Publication II © 2024 Authors).

Because of higher temperatures and higher flow rate in the bulk reduction experiments, both pellets achieved a higher reduction degree during both CO and H_2 reduction in comparison to the surface reduction. Comparing the reduction with H_2, the reduction with CO caused a significant decrease in the reduction rate and maximum reduction degree for both pellets. At 700 °C, the third stage of reduction (reduction of wüstite to iron) did not start, and the complete reduction only achieved at 1100 °C for the DRI pellet.

The pellets displayed different reduction behaviour as it was also detected during the surface reduction when CO was introduced into the system. Comparing the reduction profiles and XRD analyses reveals that at temperatures of 700 °C and 800 °C, the BF pellet exhibited a higher reduction rate compared to the DRI pellet. As the Fe_{tot} values of both pellets are very close, this disparity can be attributed to the higher concentration of magnetite in the DRI pellet (9.11%) as opposed to the BF pellet (1.93%), which renders reduction more challenging due to the presence of a dense structure and low permeability, which impedes penetration. Consequently, magnetite is preferred not to be used as a raw material in ironmaking, especially in blast furnaces (Kuila et al., 2016b; P. Li et al., 2022b; J. Yu et al., 2017). However, the magnetite formed during the first stage of reduction has a different structure, the transformation of hematite with a hexagonal crystal structure into cubic magnetite causes a volume expansion and swelling. As a result, microcracks and pores are formed as the magnetite nuclei forms, which facilitates diffusion of the reducing gas inside the ore and enhances the kinetics of reduction (Kuila et al., 2016b; J. Yu et al., 2017). Moreover, Li et al. detected a dense Fe layer with closed pores in the iron matrix when they used magnetite as a raw material for the reduction process (S. Li et al., 2022). Similar observations have been reported by other researchers, particularly at lower temperatures (Corbari & Fruehan, 2010; Edstrom, 1953; Heikkilä et al., 2020).

At 900 °C, both pellets exhibited comparable reduction behavior. Interestingly, at temperatures of 1000 °C and 1100 °C, the trend reverses, with the DRI pellet demonstrating a faster reduction rate. According to the Arrhenius equation, the diffusion coefficient rises with increasing temperature, indicating that at elevated temperatures, the reduction kinetics of BF pellets are likely not governed by slow internal diffusion.

A comparison between FESEM images suggests that elevating the temperature leads to the expansion of porosities and the development of cracks, consequently enlarging the size of porosities in both carbon monoxide and hydrogen reduction. However, this expansion is more noticeable when CO serves as the reducing agent due to its slower reduction rate compared to H_2, as reported by Turkdogan et al. and Abdelrahim et al. (Abdelrahim et al., 2020; Turkdogan & Vinters, 1971). Furthermore, the DRI pellet has fewer micropores and a more well-defined network of macropores in comparison to the BF pellet.

At 900 ℃, reduction progresses from the grain boundaries towards the grain cores in both pellets, rendering them nearly identical. While the growth of porosities and cracks was detectable since 700 ℃, a temperature increase from 900 ℃ results in a noticeable surge in porosity growth, aiding reduction. Consequently, the high porosity of the DRI pellet, which was more than the BF pellet even before the reduction according to the bulk density values, further amplified by the temperature, allows CO to diffuse easily through the pellet and react, leading to near-complete reduction at 1000 ℃. However, some wüstite remains visible in the BF pellet structure, particularly in the larger grains. At 1100 °C, a comparable scenario unfolds, wherein the DRI pellet undergoes complete reduction, whereas wüstite remains detectable in certain regions of the BF pellet structure.

Furthermore, FESEM images reveal a noteworthy observation: while many researchers have suggested that reduction initiates from the pellet surface and proceeds inward, a similar phenomenon occurs within the pellet itself, manifesting at a microscale level. Specifically, metallic iron initially forms at the grain edges and subsequently progresses towards the grain core as reduction proceeds.

4.1.2 Kinetic analysis

For each experiment, the values of α and t were inserted into various integral mechanism functions (G(α)), and the G(α) versus the t curve were derived through fitting. Concurrently, the mechanism function with the highest linearity was chosen as the most suitable. Despite the multitude of models available for iron ore reduction, this study adopts the most commonly utilized ones found in the literature (H. Chen et al., 2017; Kang et al., 2024a; P. Li et al., 2022b; X. Mao et al., 2022b; J. Zhang et al., 2024), as detailed in Table 4. It is important to note that the resistance encountered by a gas reactant passing through an ash layer is considerably greater than that through a gas film enveloping the particle. Consequently, gas film resistance may be disregarded in cases where the reaction results in the formation of a non-stripping, rigid, solid ash layer, such as during the reduction of a hematite pellet, particularly when utilizing a reducing gas with a high flow rate (Kang et al., 2024a). However, it is worth mentioning that the resistance of the ash layer remains unaffected by variations in the gas flow rate (Kang et al., 2024a).

Table 4. Kinetic models for gas-solid reactions.

Symbol	Mechanisms	G(α)
A1	1D Nucleation and growth	$-\ln(1-\alpha)$
A2	2D Nucleation and growth	$[-\ln(1-\alpha)]^{1/2}$
A3	3D Nucleation and growth	$[-\ln(1-\alpha)]^{1/3}$
D1	1D Diffusion through the solid ash	α^2
D2	2D Diffusion through the solid ash	$\alpha+(1-\alpha)\ln(1-\alpha)$
D3	3D Diffusion through the solid ash	$[1-(1-\alpha)^{1/3}]^2$
D4	3D Diffusion (Ginstling–Brounstein)	$1-3(1-\alpha)^{2/3}+2(1-\alpha)$
R1	1D Chemical reaction	α
R2	2D Chemical reaction	$1-(1-\alpha)^{1/2}$
R3	3D Chemical reaction	$1-(1-\alpha)^{1/3}$

Figure 25 illustrates the calculated results of the kinetic models outlined in Table 4. The values displayed at the top of the histogram represent the average R^2 value for each model across different temperatures. Based on the findings, it was determined that D2 (2D diffusion) exhibited the most compatibility for reducing both DRI and

BF pellets when CO served as the reducing agent, as depicted in Figure 25a and c. This suggests that the reduction process could be constrained by the rate of CO diffusion to the particle surface, with the controlling step being the diffusion of the reagent gas (CO) or product gas (CO_2) through the reduced iron layer. According to Figure 25b and d, the kinetics of the hydrogen reduction of DRI and BF pellets were controlled by A1 (1D nucleation and growth) and R3 (3D chemical reaction), respectively, which is close to the results by Kang et al. and Piotrowski et al. that reported A1 and R2 as the controlling models for the hydrogen reduction (Kang et al., 2024a; Piotrowski et al., 2005). This shows the higher diffusion capacity of H_2 which can pass through the nanoscale cracks or pores.

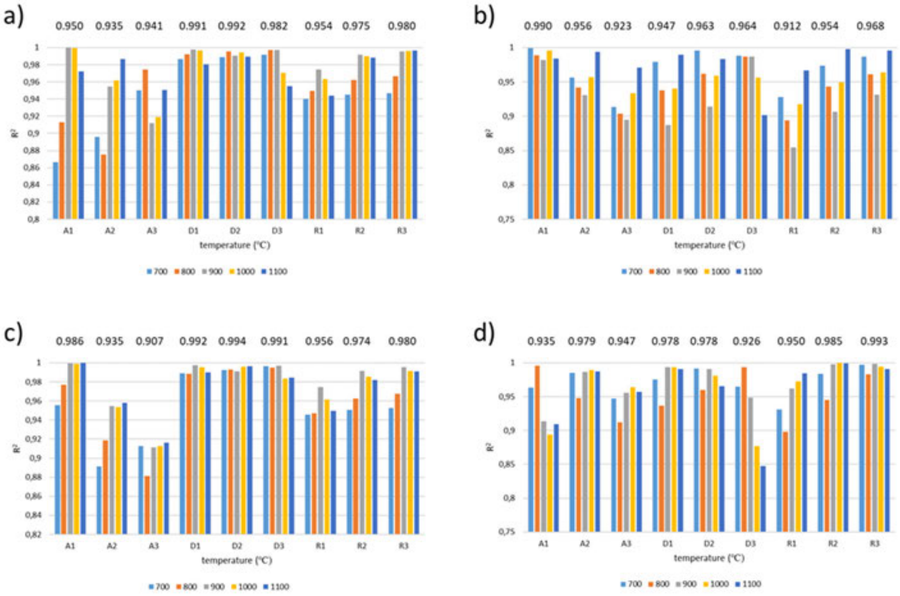

Fig. 25. Linear fitting results under different temperatures by different models for reduction of a) a DRI pellet with CO, b) a DRI pellet with H_2, c) a BF pellet with CO, and d) a BF pellet with H_2 (Reprinted under CC BY 4.0 license from Publication III © 2024 Authors).

As per Equation 4, the observable rate constant k(T) at varying temperatures was graphed against 1/T and it is illustrated in Figure 26. This resulted in a fitted line with a slope of $-E_a/R$. The apparent activation energy, E_a, was then deduced from the slope, and the pre-exponential factor, A, was computed using the intercept.

Consequently, the kinetic triplets, which include E_a, A, and G(α), were established and are shown in Table 5.

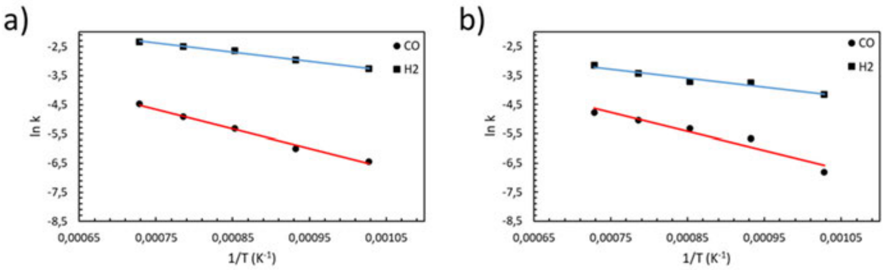

Fig. 26. Arrhenius plot for the reduction rate constant of a) a DRI pellet, and b) a BF pellet with H_2 and CO (Reprinted under CC BY 4.0 license from Publication III © 2024 Authors).

Table 5. The E_a and A, derived from Arrhenius plots for different reduction conditions.

Reduction conditions	DRI pellet reduced by H_2	BF pellet reduced by H_2	DRI pellet reduced by CO	BF pellet reduced by CO
Kinetic models	A1	R3	D2	D2
E_a (kJ.mol^{-1})	26.12	25.71	55.59	53.80
A (min^{-1})	0.98	0.38	1.43	1.08

According to the data presented in Table 5, the activation energy decreased from 55.59 kJ/mol and 53.80 kJ/mol to 26.12 kJ/mol and 25.71 kJ/mol, respectively, when transitioning from carbon monoxide to hydrogen as the reducing gas. This observation suggests the enhanced diffusion capability of hydrogen, enabling more hydrogen molecules to surmount the energy barrier required for initiating the reaction. Furthermore, the comparable activation energy values observed for pellets reduced in the same gas indicate that the influence of the gas composition outweighs the impact of pellet properties such as mineralogy and porosity.

To gain a more precise understanding of pellet porosity, microtomography tests were conducted, as shown in Figure 27. An ImageJ software analysis revealed that the porosity of unreduced BF and DRI pellets was 32% and 38%, respectively. Surface areas were also calculated using the Brunauer-Emmett-Teller (BET) equation, with values of 0.064 m^2/g for BF pellets and 0.069 m^2/g for DRI pellets. The higher porosity and surface area of DRI pellets suggest more and larger pores compared to BF pellets, facilitating CO diffusion and improving reducibility, particularly at higher temperatures.

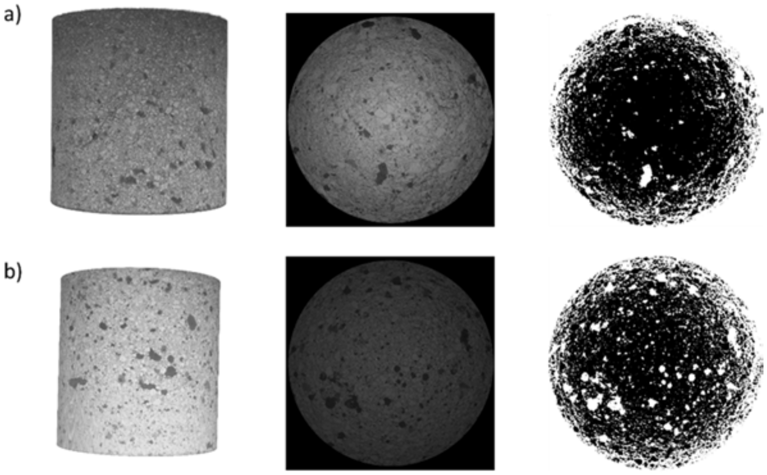

Fig. 27. From left to right: 3D, 2D, and processed microtomography images of a) an unreduced BF pellet, and b) an unreduced DRI pellet (Reprinted under CC BY 4.0 license from Publication III © 2024 Authors).

4.2 The effect of water vapor on the reduction

4.2.1 Reduction and microstructure

As shown in the previous chapter, adding water vapor to the gas mixture not only decreases the rate of reduction, but also affects the maximum reduction degree depending on the percentage of water vapor. Adding 10% water vapor did not have a significant effect on the maximum reduction degree. However, adding 20% water vapor to the system resulted in a notable drop of the maximum reduction degree to 36% and 77% at 800 °C and 900 °C, respectively.

The Baur–Glaessner diagram suggests that complete reduction should occur at a thermodynamic equilibrium even with 30% water vapor in the system. However, the reduction curves and FESEM images indicate the presence of a kinetic barrier that prevents full reduction, as the transformation of wüstite to metallic iron did not commence.

A closer analysis reveals that as the partial pressure of water vapor (P_{H2O}) increased, the pellet grain size expanded, while the number and size of micro-pores diminished. This structural change heightened diffusion resistance, making it more difficult for hydrogen to penetrate the pellet core and for the water vapor generated during reduction to escape to the surface. Additionally, as the reduction progressed, the formation of a solid iron layer on the pellet surface further extended the diffusion pathway. This meant that hydrogen had to travel a greater distance from the surface to the iron/wüstite interface, and the water vapor had to diffuse farther in the opposite direction, increasing the resistance to mass transfer.

However, the absence of metallic iron on the pellet surface when 30% water vapor was present suggests that these factors alone do not fully account for the hindered reduction. A key contributing factor appears to be the concentration gradient, which drives diffusion. When the water vapor content in the gas mixture increases while maintaining constant total pressure, the partial pressure of hydrogen decreases, effectively diluting its concentration in the reactive gas. This weakens the hydrogen concentration gradient between the reaction interface and the pellet surface. Simultaneously, the elevated water vapor concentration at the pellet surface reduces its gradient between the reaction site (where it is produced) and the surface, further impeding diffusion.

Thus, the primary reason for the decline in reduction efficiency at higher water vapor levels is the reduction in concentration gradients for both hydrogen and water vapor, which significantly limits mass transport and reaction kinetics.

4.2.2 Kinetic analysis

As previously mentioned, the reduction process occurs in three sequential stages: hematite (Fe_2O_3) to magnetite (Fe_3O_4), magnetite to wüstite (FeO), and wüstite to metallic iron (Fe). Therefore, the kinetics of each stage should be analyzed separately. However, since the transformation of Fe_2O_3 to Fe_3O_4 occurs extremely rapidly, it could not be distinctly identified for kinetic analysis. As a result, the first two stages were combined, and the overall reaction $Fe_2O_3 \rightarrow FeO$ was considered as the first stage of reduction.

A common approach for determining isothermal kinetic parameters involves fitting experimental data to theoretical models. By comparing experimental results with model predictions, the most suitable model is identified based on the smallest deviation in conversion rates. For each experiment, the degree of reduction (α) and time (t) were applied to various integral mechanism functions, generating $G(\alpha)$ vs.

t curves through data fitting. The model that demonstrated the highest linearity was selected as the most appropriate.

While numerous models exist for iron ore reduction, this study focused on those most commonly used in the literature (H. Chen et al., 2017; Garg et al., 2022; Kang et al., 2024a; P. Li et al., 2022b; X. Mao et al., 2022b; J. Zhang et al., 2024), as summarized in Table 4.

It is important to note that gas resistance when passing through an ash layer is significantly higher than the resistance of the gas film surrounding the particle. In reduction processes that produce a solid, non-porous ash layer, such as in hematite pellet reduction, gas film resistance can be considered negligible—especially when a reducing gas with a high flow rate is used (Kang et al., 2024a).

The model fitting for the first stage of reduction is presented in Figure 28. As shown in Figure 28, when pure hydrogen is used at all temperatures, as well as when 10% water vapor is introduced at 900 °C and 1000 °C, the primary resistance to reduction is attributed to the chemical reaction. However, for reduction with 10% water vapor at 800 °C and 20% water vapor at 900 °C and 1000 °C, the controlling mechanism shifts to diffusion.

In contrast, when using 20% water vapor at 800 °C and 30% water vapor across all temperatures, none of the models listed in Table 6 exhibited strong linearity, suggesting that no single mechanism fully captures the kinetics under these conditions. This indicates that the reduction process is likely governed by a combination of factors—a phenomenon known as mixed-control kinetics.

In other words, at low water vapor concentrations, hydrogen readily diffuses into the pellets, making the reduction primarily reaction controlled. However, as the water vapor content increases or the temperature decreases, diffusion becomes more restricted. As previously discussed, higher water vapor levels reduce the concentration gradient, which is the driving force for diffusion. Additionally, excessive water vapor further inhibits the chemical reaction by blocking active sites at the reaction interface (Moukassi et al., 1983; Spreitzer & Schenk, 2019b). The surface of wüstite is considered to have a limited number of available sites for hydrogen and water vapor adsorption. Additionally, water vapor can dissociate into oxygen ions and hydrogen at the wüstite surface, as described by reaction 36. As a result, in addition to water vapor and hydrogen, the oxygen produced from reaction 36 can also occupy these surface sites on wüstite (Turkdogan et al., n.d.).

$$H_2O(g) + 2e \longrightarrow O^{2-} + H_2(g). \tag{36}$$

Equation 37 represents the total number of available sites on the surface of wüstite, expressed as:

$$\theta_{H_2O} + \theta_{H_2} + \theta_O + \theta_\Psi + \theta_\square = 1, \tag{37}$$

where θ_{H2O}, θ_{H2}, and θ_O denote the fraction of surface sites occupied by water vapor, hydrogen, and oxygen molecules, respectively. θ_Ψ represents the fraction of sites occupied by the activated complex, and $\theta_\square$ corresponds to the fraction of vacant surface sites.

A water vapor molecule can form an activated complex on the wüstite surface according to reaction 38

$$H_2O(g) \longrightarrow [H_2O]_\Psi. \tag{38}$$

The equilibrium constant for reaction 38, K_Ψ, is given by Equation 39:

$$K_\Psi = \frac{a_\Psi}{a_{H_2O}}, \tag{39}$$

where a_Ψ and a_{H2O} are the activity of activated complex and water vapor respectively. The activity values of activated complex and oxygen at the surface of wüstite (oxide-gas surface) can be calculated using Equations 40 and 41:

$$a_O = k_1 \frac{\theta_O}{\theta_\square} \tag{40}$$

and

$$a_\Psi = k_2 \frac{\theta_\Psi}{\theta_\square}, \tag{41}$$

where k_1 and k_2 are proportionality factors that depend on temperature.

By substituting Equations 40 and 41 into Equation 39 and replacing a_{H2O} with the partial pressure of water vapor, the fraction of sites occupied by the activated complex can be expressed as Equation 42:

$$\theta_\Psi = K_\Psi \frac{k_1}{k_2} \frac{\theta_O}{a_O} p_{H_2O}. \tag{42}$$

Equation 42 reveals that an increase in water vapor partial pressure leads to a higher fraction of surface sites being occupied by the activated complex. This blocks the interaction between hydrogen and wüstite, thereby hindering the reduction of wüstite by hydrogen.

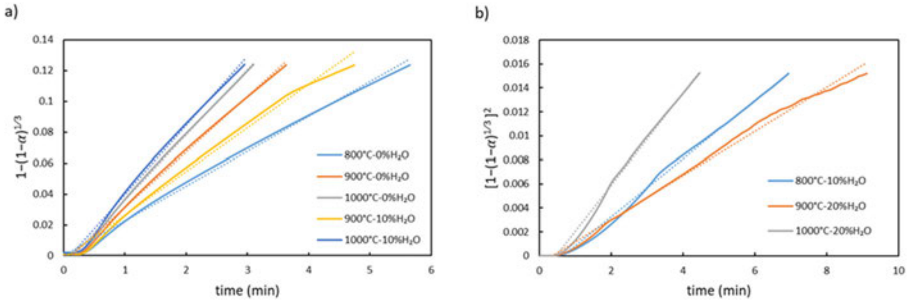

Fig. 28. Model fitting for the first stage of reduction a) 3D chemical reaction (R3), and b)3D diffusion (D3) (Reprinted under CC BY 4.0 license from Publication IV © 2025 Authors).

According to the Arrhenius equation, the observable rate constant k(T) form R3 and D3 models was plotted against 1/T for different temperatures, as illustrated in Figure 29. This plot produced a linear relationship, with the slope corresponding to $-E_a/R$. Using this slope, the activation energy (E_a) was determined to be 49.09, 169.14, 169.12, and 72.45 kJ/mol for reductions with 0%, 10%, 20%, and 30% water vapor, respectively. These values are consistent with those reported in previous studies (Heidari et al., 2021). Mao et al. established a correlation between activation energy and the rate-controlling mechanism, as summarized in Table 6 (X. D. Mao et al., 2023). Based on this classification, the activation energy values for reductions with 10% and 20% water vapor correspond to the range typically associated with solid-state diffusion, whereas the value for 30% water vapor falls between interfacial chemical reaction and solid-state diffusion. These findings align well with the results obtained from kinetic model fitting, further supporting the proposed reaction mechanisms.

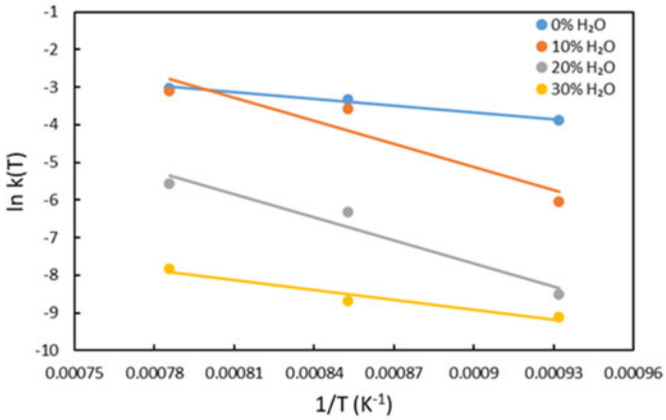

Fig. 29. Arrhenius plots for the first stage of reduction (Reprinted under CC BY 4.0 license from Publication IV © 2025 Authors).

Table 6. Relationship between apparent activation energy and probable rate controlling model.

Apparent activation energy E_a (kJ/mol)	Probable rate controlling model
8~16	Gas diffusion
29~42	Combined gas diffusion and interfacial chemical reaction
60~67	Interfacial chemical reaction
>90	Solid-state diffusion

A similar method was applied to determine the rate-controlling mechanism for the second stage of reduction, with the model fitting results illustrated in Figure 30. Similar to Bonalde et al. resalts, the 3D diffusion model (D3) exhibited the best linearity for reduction in pure hydrogen at 800 °C and 900 °C, which can be attributed to the formation of a solid metallic iron layer on the pellet surface that restricts diffusion (BONALDE et al., 2005). However, at 1000 °C, the controlling mechanism transitioned to a chemical reaction, as the higher temperature facilitated hydrogen diffusion.

For reduction with 10% water vapor, diffusion remained the dominant mechanism at 800 °C and 900 °C. However, at 1000 °C, none of the models from Table 4 provided a perfect fit, indicating that the process was likely mix-controlled, involving both diffusion and chemical reaction.

When using 20% water vapor at 900 °C and 1000 °C, diffusion continued to be the rate-controlling step. Although higher temperatures improve hydrogen diffusion within the pellet, the increased water vapor content reduces the concentration gradient, thereby impeding diffusion. Consequently, even at 1000 °C with 20% water vapor, diffusion remains the primary rate-controlling mechanism.

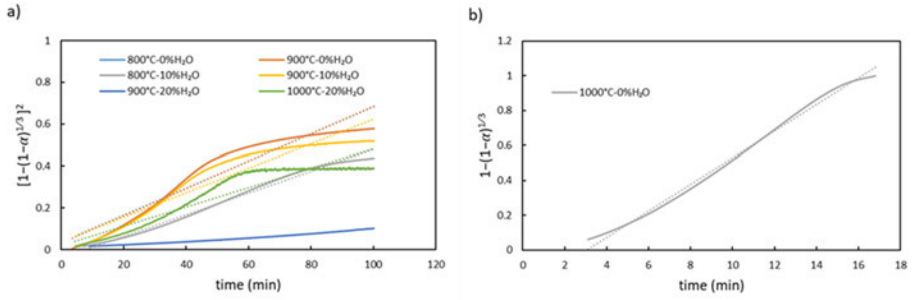

Fig. 30. Model fitting for the second stage of reduction a) 3D diffusion (D3), and b) 3D chemical reaction (R3) (Reprinted under CC BY 4.0 license from Publication IV © 2025 Authors).

The Arrhenius plots for the second stage of reduction are shown in Figure 31. Analysis of the slope revealed activation energy values of 134.65, 145.89, and 177.40 kJ/mol for reductions with 0%, 10%, and 20% water vapor, respectively. These results indicate that an increase in water vapor content corresponds to higher activation energy.

Furthermore, when compared to the data in Table 6, the obtained activation energy values fall within the range typically associated with solid-state diffusion. This behavior is attributed to the formation of a solid metallic iron layer on the pellet surface, which acts as a diffusion barrier.

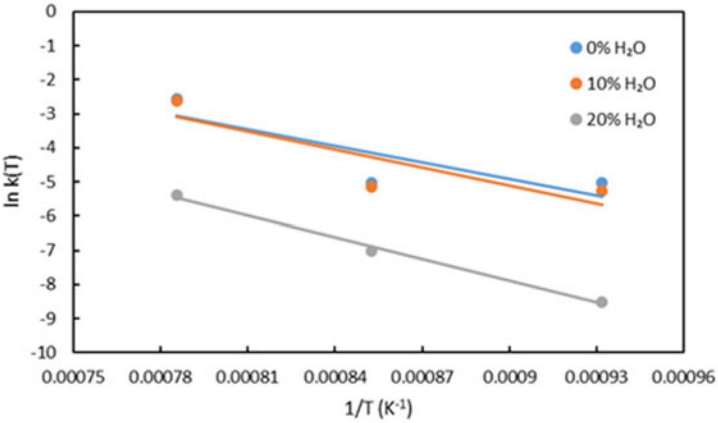

Fig. 31. Arrhenius plots for the second stage of reduction (Reprinted under CC BY 4.0 license from Publication IV © 2025 Authors).

5 Conclusion

5.1 Conclusion

This research provides a comprehensive analysis of the hydrogen reduction of iron ore pellets, with a particular focus on both direct reduced iron (DRI) and blast furnace (BF) pellets. The study examines the surface and bulk reduction behaviors under different conditions, evaluating the effects of hydrogen (H_2), carbon monoxide (CO), and water vapor (H_2O) on the reduction kinetics, phase transformation, and microstructural evolution.

The results reveal that DRI pellets achieve a higher metallization degree compared to BF pellets during surface reduction with hydrogen, owing to their greater porosity, which enhances gas diffusion. Although the introduction of carbon monoxide into the system stopped the reduction of DRI pellets, BF pellets exhibit partial reduction when exposed to a CO-H_2 mixture, but their surface is prone to reoxidation due to the accumulation of water vapor and CO_2, particularly at low gas flow rates.

In bulk reduction experiments, both DRI and BF pellets were tested using pure hydrogen and pure carbon monoxide at temperatures ranging from 700 °C to 1100 °C. The results indicate that reduction is significantly faster with hydrogen than with carbon monoxide due to hydrogen's smaller molecular size and higher diffusion coefficient. Both pellets reached near-complete reduction with hydrogen at high temperatures, whereas carbon monoxide reduction was considerably slower, particularly at 700–800 °C, where the final step of wüstite to iron transformation did not occur. At 700°C and 800 °C, BF pellets underwent faster and more extensive reduction than DRI pellets when using CO as the reducing agent. This difference is primarily due to the higher magnetite content in DRI pellets, which makes reduction more challenging. However, at 1000 °C and 1100 °C, the trend reversed, with DRI pellets displaying higher reduction rates than BF pellets. This shift can be attributed to the greater porosity and larger pore structures in DRI pellets, which enhance gas diffusion and reaction kinetics.

The effect of water vapor on hydrogen reduction was also investigated, showing that although complete reduction is thermodynamically possible even with 30% water vapor, the kinetic barrier prevents the final step of wüstite to iron transformation. Increasing water vapor content decreases the hydrogen concentration gradient, blocks active reaction sites, and shifts the rate-controlling mechanism from chemical reaction control to diffusion control. However, at 10% water vapor, the reduction degree remains largely unaffected, while at 20% and higher levels, a significant decline is observed, particularly at lower temperatures.

A kinetic analysis revealed that the rate-controlling mechanisms depend on both temperature and gas composition. When using pure hydrogen, reduction is primarily governed by chemical reaction along with nucleation and growth processes. In contrast, when CO serves as the reducing agent, the process is diffusion-controlled, particularly at lower temperatures, due to the slower diffusion rate of CO compared to H_2. An Arrhenius analysis further validated these findings, with activation energy values consistent with those reported for solid-state diffusion in iron oxide reduction. The introduction of water vapor led to a mixed-control mechanism, where active site blockage on wüstite increased the chemical reaction resistance, while a decreased concentration gradient intensified the diffusion resistance, further hindering the reduction process.

Overall, this study provides critical insights into the mechanisms, kinetics, and microstructural transformations involved in hydrogen-based and CO-based reduction of iron ore pellets. The findings highlight the advantages of hydrogen reduction, while also identifying challenges related to diffusion barriers, water vapor effects, and reoxidation risks. These results contribute to the ongoing transition toward fossil-free steel production, offering valuable guidance for optimizing hydrogen-based direct reduction processes in industrial applications.

5.2 Future work

To address existing research gaps and build upon previous findings, the following areas are recommended for future investigation:

- **High-Temperature Surface Reduction:** Conduct APXPS experiments at elevated temperatures (800–1000 °C) to better understand surface reduction mechanisms.
- **Pellet Size Effects:** Analyze the impact of pellet size through single-pellet reduction tests and batch reduction experiments to evaluate scalability.
- **Dynamic Reduction Simulations:** Simulate hydrogen reduction in a shaft furnace using dynamic reduction tests across different scales to mimic industrial conditions.

- **Parameter Interactions:** Investigate how flow rate, pressure, and porosity interact with water vapor during hydrogen reduction and their influence on reaction kinetics.
- **Melting Behavior Analysis:** Examine the melting characteristics of pellets reduced under different conditions using an EAF simulator to assess their suitability for steelmaking.

These future studies will provide deeper insights into the hydrogen-based reduction process, supporting the transition toward sustainable ironmaking.

List of references

Abdel Halim, K. S., El-Geassy, A. A., Nasr, M. I., Ramadan, M., Fathy, N., & Al-Ghamdi, A. S. (2023). Characteristics and applications of iron oxide reduction processes. *Polish Journal of Chemical Technology*, *25*(4), 81–92. https://doi.org/doi:10.2478/pjct-2023-0041

Abdelrahim, A., Iljana, M., Omran, M., Vuolio, T., Bartusch, H., & Fabritius, T. (2020). Influence of H2–H2O content on the reduction of acid iron ore pellets in a CO–CO2–N2 reducing atmosphere. *ISIJ International*, *60*(10), 2206–2217. https://doi.org/10.2355/isijinternational.ISIJINT-2019-734

Adam, F., Dupré, B., & Gleitzer, C. (1989). The role of water in the low-temperature hydrogen reduction of hematite into iron, and the role of the surface oxygen chemical potential in double reactions. *Reactivity of Solids*, *7*(4), 383–397. https://doi.org/10.1016/0168-7336(89)80059-2

Angalakuditi, V. B., Bhadravathi, P., Gujare, R., Ayyappan, G., Singh, L. R., & Baral, S. S. (2022). Mineralogical Aspects of Reducing Lump Iron Ore, Pellets, and Sinter with Hydrogen. *Metallurgical and Materials Transactions B: Process Metallurgy and Materials Processing Science*, *53*(2), 1036–1065. https://doi.org/10.1007/s11663-022-02442-4

Bahgat, M., Abdel Halim, K. S., Nasr, M. I., & El-Geassy, A. A. (2008). Morphological changes accompanying gaseous reduction of SiO2 doped wüstite. *Ironmaking and Steelmaking*, *35*(3), 205–212. https://doi.org/10.1179/174328107X155259

Bahgat, M., Abdel Halim, K. S., Nasr, M. I., & El-Geassy, A. H. A. (2007). Reduction behaviour of wüstite doped with MgO. *Steel Research International*, *78*(6), 443–450. https://doi.org/10.1002/srin.200706228

Bahgat, M., & Khedr, M. H. (2007). Reduction kinetics, magnetic behavior and morphological changes during reduction of magnetite single crystal. *Materials Science and Engineering: B*, *138*(3), 251–258. https://doi.org/10.1016/j.mseb.2007.01.029

BONALDE, A., HENRIQUEZ, A., & MANRIQUE, M. (2005). Kinetic Analysis of the Iron Oxide Reduction Using Hydrogen-Carbon Monoxide Mixtures as Reducing Agent. *ISIJ International*, *45*(9), 1255–1260. https://doi.org/10.2355/isijinternational.45.1255

Cavaliere, P., Dijon, L., Laska, A., & Koszelow, D. (2023). Hydrogen direct reduction and reoxidation behaviour of high-grade pellets. *International Journal of Hydrogen Energy*, *xxxx*. https://doi.org/10.1016/j.ijhydene.2023.08.254

Chen, F., Mohassab, Y., Jiang, T., & Sohn, H. Y. (2015). Hydrogen Reduction Kinetics of Hematite Concentrate Particles Relevant to a Novel Flash Ironmaking Process. *Metallurgical and Materials Transactions B*, *46*(3), 1133–1145. https://doi.org/10.1007/s11663-015-0332-z

Chen, H., Zheng, Z., Chen, Z., & Bi, X. T. (2017). Reduction of hematite (Fe2O3) to metallic iron (Fe) by CO in a micro fluidized bed reaction analyzer: A multistep kinetics study. *Powder Technology*, *316*, 410–420. https://doi.org/10.1016/j.powtec.2017.02.067

Corbari, R., & Fruehan, R. J. (2010). Reduction of iron oxide fines to wustite with CO/CO2 gas of low reducing potential. *Metallurgical and Materials Transactions B, 41*(2), 318–329. https://doi.org/10.1007/s11663-009-9315-2

Du, W., Yang, S., Pan, F., Shangguan, J., Lu, J., Liu, S., & Fan, H. (2017). Hydrogen Reduction of Hematite Ore Fines to Magnetite Ore Fines at Low Temperatures. *Journal of Chemistry*, *2017*. https://doi.org/10.1155/2017/1919720

Edstrom, J. O. (1953). The mechanism of reduction of iron oxides. *Journal of the Iron and Steel Institute*, *175*(3), 289.

Garg, P., Hu, X., Li, Y., Li, K., Nag, S., & Zhang, J. (2022). Kinetics of Iron Oxide Reduction in H 2/ H 2O Gas Mixture: Global and Stepwise Reduction. *Metallurgical and Materials Transactions B: Process Metallurgy and Materials Processing Science*, *53*(3), 1759–1774. https://doi.org/10.1007/s11663-022-02485-7

Habermann, A., Winter, F., Hofbauer, H., Zirngast, J., & Schenk, J. L. (2000). Experimental study on the kinetics of fluidized bed iron ore reduction. *ISIJ International*, *40*(10), 935–942. https://doi.org/10.2355/isijinternational.40.935

Han, Y., Zhang, H., Yu, Y., & Liu, Z. (2021). In Situ Characterization of Catalysis and Electrocatalysis Using APXPS. *ACS Catalysis*, *11*(3), 1464–1484. https://doi.org/10.1021/acscatal.0c04251

Heidari, A., Niknahad, N., Iljana, M., & Fabritius, T. (2021). A review on the kinetics of iron ore reduction by hydrogen. *Materials*, *14*(24). https://doi.org/10.3390/ma14247540

Heikkilä, A., Iljana, M., Bartusch, H., & Fabritius, T. (2020). Reduction of Iron Ore Pellets, Sinter, and Lump Ore under Simulated Blast Furnace Conditions. *Steel Research International*, *91*(11). https://doi.org/10.1002/srin.202000047

Hölling, M., & Gellert, S. (2018). Direct Reduction: Transition from Natural Gas to Hydrogen? *Icsti 2018*, *September*. https://www.researchgate.net/publication/327962750_Direct_Reduction_Transition_from_Natural_Gas_to_Hydrogen

Hou, B., Zhang, H., Li, H., & Zhu, Q. (2012). Study on kinetics of iron oxide reduction by hydrogen. *Chinese Journal of Chemical Engineering*, *20*(1), 10–17. https://doi.org/10.1016/S1004-9541(12)60357-7

Iguchi, Y., Fukunaga, M., & Hirao, J. (1982). Dependences of the Reduction Rate of Wustite Containing CaO on the Reduction Temperature and α-γ Transformation of Metallic Iron. *Journal of the Japan Institute of Metals and Materials*, *46*(8), 780–786. https://doi.org/https://doi.org/10.2320/jinstmet1952.46.8_780

Kang, H., Xu, Q., Cao, Z., Lu, X., Shi, J., Chen, B., & Guo, L. (2023). Influence of hydrogen flow rate on multistep kinetics of hematite reduction. *International Journal of Hydrogen Energy*, *xxxx*. https://doi.org/10.1016/j.ijhydene.2023.08.295

Kang, H., Xu, Q., Cao, Z., Lu, X., Shi, J., Chen, B., & Guo, L. (2024). Influence of hydrogen flow rate on multistep kinetics of hematite reduction. *International Journal of Hydrogen Energy*, *49*(xxxx), 1255–1268. https://doi.org/10.1016/j.ijhydene.2023.08.295

Kapelyushin, Y., Xing, X., Zhang, J., Jeong, S., Sasaki, Y., & Ostrovski, O. (2015). Effect of Alumina on the Gaseous Reduction of Magnetite in CO / CO 2 Gas Mixtures. *Metallurgical and Materials Transactions B, May 2016*. https://doi.org/10.1007/s11663-015-0316-z

Kar, M. K., Zhu, M., & Safarian, J. (2023). Comparative kinetics study of different iron-containing pellets with hydrogen at isothermal conditions. *Journal of Materials Research and Technology*, *27*(September), 8062–8072. https://doi.org/10.1016/j.jmrt.2023.11.248

Kawasaki, E., Sanscrainte, J., & Walsh, T. J. (1962). Kinetics of reduction of iron oxide with carbon monoxide and hydrogen. *AIChE Journal*, *8*(1), 48–52. https://doi.org/https://doi.org/10.1002/aic.690080114

Kazemi, M., Pour, M. S., & Sichen, D. (2017). Experimental and Modeling Study on Reduction of Hematite Pellets by Hydrogen Gas. *Metallurgical and Materials Transactions B: Process Metallurgy and Materials Processing Science*, *48*(2), 1114–1122. https://doi.org/10.1007/s11663-016-0895-3

Kim, W. H., Lee, Y. S., Suh, I. K., & Min, D. J. (2012). Influence of CAO and Sio 2 on the reducibility of wüstite using H 2 and co gas. *ISIJ International*, *52*(8), 1463–1471. https://doi.org/10.2355/isijinternational.52.1463

Kokkonen, E., Da Silva, F. L., Mikkela, M. H., Johansson, N., Huang, S. W., Lee, J. M., Andersson, M., Bartalesi, A., N. Reinecke, B., Handrup, K., Tarawneh, H., Sankari, R., Knudsen, J., Schnadt, J., Sathe, C., & Urpelainen, S. (2021). Upgrade of the SPECIES beamline at the MAX IV Laboratory. *Journal of Synchrotron Radiation*, *28*(November 2020), 588–601. https://doi.org/10.1107/S1600577521000564

Korobeinikov, Y., Meshram, A., Harris, C., Kovtun, O., Govro, J., O'Malley, R. J., Volkova, O., & Sridhar, S. (2023). Reduction of Iron-Ore Pellets Using Different Gas Mixtures and Temperatures. *Steel Research International*, *94*(10). https://doi.org/10.1002/srin.202300066

Kuila, S. K., Chatterjee, R., & Ghosh, D. (2016). Kinetics of hydrogen reduction of magnetite ore fines. *International Journal of Hydrogen Energy*, *41*(22), 9256–9266. https://doi.org/10.1016/j.ijhydene.2016.04.075

Kushnir, D., Hansen, T., Vogl, V., & Åhman, M. (2020). Adopting hydrogen direct reduction for the Swedish steel industry: A technological innovation system (TIS) study. *Journal of Cleaner Production*, *242*, 118185. https://doi.org/10.1016/j.jclepro.2019.118185

Li, P., Li, Y., Yu, J., Gao, P., & Han, Y. (2022). Kinetics and microstructural changes during fluidized reduction of magnetite with hydrogen at low temperatures. *International Journal of Hydrogen Energy*, *47*(73), 31140–31151. https://doi.org/10.1016/j.ijhydene.2022.07.032

Li, S., Gu, H., Huang, A., Zou, Y., Yang, S., & Fu, L. (2022). Thermodynamic analysis and experimental verification of the direct reduction of iron ores with hydrogen at elevated temperature. *Journal of Materials Science*, *57*(43), 20419–20434. https://doi.org/10.1007/s10853-022-07855-9

Li, S., Zhang, H., Nie, J., Dewil, R., Baeyens, J., & Deng, Y. (2021). The direct reduction of iron ore with hydrogen. *Sustainability (Switzerland)*, *13*(16), 1–16. https://doi.org/10.3390/su13168866

Lu, X., Xu, Q., Kang, H., Shi, J., Cao, Z., Chen, B., & Guo, L. (2024). Multistep kinetic study of magnetite reduction by hydrogen based on thermogravimetric analysis. *International Journal of Hydrogen Energy*, *73*(June), 695–707. https://doi.org/10.1016/j.ijhydene.2024.06.081

Mao, X. D., Hu, X. J., Fan, Y. W., & Chou, K. C. (2023). Effect of Water Vapor on the Reduction Kinetics of Hematite Powder By Hydrogen-Water Vapor in Different Stages. *Journal of Mining and Metallurgy, Section B: Metallurgy*, *59*(1), 65–76. https://doi.org/10.2298/JMMB220523006M

Mao, X., Garg, P., Hu, X., Li, Y., Nag, S., Kundu, S., & Zhang, J. (2022). Kinetic analysis of iron ore powder reaction with hydrogen—carbon monoxide. *International Journal of Minerals, Metallurgy and Materials*, *29*(10), 1882–1890. https://doi.org/10.1007/s12613-022-2512-6

Metolina, P., Ribeiro, T. R., & Guardani, R. (2022). Hydrogen-based direct reduction of industrial iron ore pellets: Statistically designed experiments and computational simulation. *International Journal of Minerals, Metallurgy and Materials*, *29*(10), 1908–1921. https://doi.org/10.1007/s12613-022-2487-3

Mishra, B., Kumar Singh, A., & Shankar Mahobia, G. (2024). Hydrogen reduction studies of low-grade multimetallic magnetite ore pellets. *Minerals Engineering*, *215*(February), 108823. https://doi.org/10.1016/j.mineng.2024.108823

Monazam, E. R., Breault, R. W., & Siriwardane, R. (2014). Kinetics of hematite to wüstite by hydrogen for chemical looping combustion. *Energy and Fuels*, *28*(8), 5406–5414. https://doi.org/10.1021/ef501100b

Moukassi, M., Steinmetz, P., Dupre, B., & Gleitzer, C. (1983). A study of the mechanism of reduction with hydrogen of pure wustite single crystals. *Metallurgical Transactions B*, *14*(1), 125–132. https://doi.org/10.1007/BF02670879

Nie, T., Xu, Q., She, Y., Ye, X., Wang, M., Luo, X., & Guo, L. (2024). The behavior of surface nanobubbles on different substrates in electrochemistry. *Journal of Molecular Liquids*, *394*. https://doi.org/10.1016/j.molliq.2023.123791

Ohmi, M., & Usui, T. (1982). Improved Theory on the Rate of Reduction of Single Particles and Fixed Bed of Iron Oxide Pellets With Hydrogen. *Transactions of the Iron and Steel Institute of Japan*, *22*(1), 66–74. https://doi.org/10.2355/isijinternational1966.22.66

Ohmi, M., Usui, T., Naito, M., & Minamide, Y. (1983). *Experimental Study of the Resistance due to the Rate of Gas Flow on the Hydrogen Reduction of an Iron Oxide Pellet**.

Özgün, Ö., Dirba, I., Gutfleisch, O., Ma, Y., & Raabe, D. (2024). Green Ironmaking at Higher H2 Pressure: Reduction Kinetics and Microstructure Formation During Hydrogen-Based Direct Reduction of Hematite Pellets. *Journal of Sustainable Metallurgy*, *0123456789*. https://doi.org/10.1007/s40831-024-00877-4

Pan, F., Zhu, Q., Du, Z., & Sun, H. (2018). Migration behavior of the MgO and its influence on the reduction of Fe3O4-MgO sinter. In *ISIJ International* (Vol. 58, Issue 4, pp. 652–659). Iron and Steel Institute of Japan. https://doi.org/10.2355/isijinternational.ISIJINT-2017-566

Pineau, A., Kanari, N., & Gaballah, I. (2006). Kinetics of reduction of iron oxides by H2. Part I: Low temperature reduction of hematite. *Thermochimica Acta*, *447*(1), 89–100. https://doi.org/10.1016/j.tca.2005.10.004

Pineau, A., Kanari, N., & Gaballah, I. (2007). Kinetics of reduction of iron oxides by H2. Part II. Low temperature reduction of magnetite. *Thermochimica Acta*, *456*(2), 75–88. https://doi.org/10.1016/j.tca.2007.01.014

Piotrowski, K., Mondal, K., Lorethova, H., Stonawski, L., Szymański, T., & Wiltowski, T. (2005). Effect of gas composition on the kinetics of iron oxide reduction in a hydrogen production process. *International Journal of Hydrogen Energy*, *30*(15), 1543–1554. https://doi.org/10.1016/j.ijhydene.2004.10.013

Pousette, H., Kojola, N., & Hessling, O. (2024). Reduction and Carburization Mechanisms for CO + H2 Reduction in Shaft Furnace Conditions. *Metallurgical and Materials Transactions B: Process Metallurgy and Materials Processing Science*. https://doi.org/10.1007/s11663-024-03235-7

Raabe, D., Klug, M. J., Ma, Y., Büyükuslu, Ö., Springer, H., & Souza Filho, I. (2023). *Hydrogen Plasma Reduction of Iron Oxides* (C. Fleuriault, J. D. Steenkamp, D. Gregurek, J. F. White, Q. G. Reynolds, P. J. Mackey, & S. A. C. Hockaday, Eds.; pp. 83–84). Springer Nature Switzerland. https://doi.org/10.1007/978-3-031-22634-2_7

Redekop, E. A., Johansson, N., Kokkonen, E., Urpelainen, S., Lopes da Silva, F., Kaipio, M., Nieminen, H.-E., Rehman, F., Miikkulainen, V., Ritala, M., & Olsbye, U. (2021). Synchronizing gas injections and time-resolved data acquisition for perturbation-enhanced APXPS experiments. *Review of Scientific Instruments*, *92*(4), 44101. https://doi.org/10.1063/5.0039957

Rukini, A., Rhamdhani, M. A., Brooks, G. A., & Van den Bulck, A. (2022). Metals Production and Metal Oxides Reduction Using Hydrogen: A Review. *Journal of Sustainable Metallurgy*, *8*(1), 1–24. https://doi.org/10.1007/s40831-021-00486-5

Scharm, C., Küster, F., Laabs, M., Huang, Q., Volkova, O., Reinmöller, M., Guhl, S., & Meyer, B. (2022). Direct reduction of iron ore pellets by H2 and CO: In-situ investigation of the structural transformation and reduction progression caused by atmosphere and temperature. *Minerals Engineering*, *180*. https://doi.org/10.1016/j.mineng.2022.107459

Seth, B. B. L., & Ross, H. U. (1963). The effect of lime on the reducibility of iron-oxide agglomerates. *Canadian Metallurgical Quarterly*, *2*(1), 15–30. https://doi.org/10.1179/cmq.1963.2.1.15

Shigematsu, N., & Iwai, H. (1987). Effect of the Addition of Al2O3 and Al2O3-Ca0 on the Reduction of Dense Wustite with H2. *Tetsu-to-Hagane*, *73*(16), 2243–2250. https://doi.org/10.2355/tetsutohagane1955.73.16_2243

Souza Filho, I. R., Ma, Y., Kulse, M., Ponge, D., Gault, B., Springer, H., & Raabe, D. (2021). Sustainable steel through hydrogen plasma reduction of iron ore: Process, kinetics, microstructure, chemistry. *Acta Materialia*, *213*. https://doi.org/10.1016/j.actamat.2021.116971

Souza Filho, I. R., Ma, Y., Raabe, D., & Springer, H. (2023). Fundamentals of Green Steel Production: On the Role of Gas Pressure During Hydrogen Reduction of Iron Ores. *Jom*, *75*(7), 2274–2286. https://doi.org/10.1007/s11837-023-05829-z

Souza Filho, I. R., Springer, H., Ma, Y., Mahajan, A., da Silva, C. C., Kulse, M., & Raabe, D. (2022). Green steel at its crossroads: Hybrid hydrogen-based reduction of iron ores. *Journal of Cleaner Production*, *340*(February). https://doi.org/10.1016/j.jclepro.2022.130805

Spreitzer, D., & Schenk, J. (2019a). Iron Ore Reduction by Hydrogen Using a Laboratory Scale Fluidized Bed Reactor: Kinetic Investigation—Experimental Setup and Method for Determination. *Metallurgical and Materials Transactions B: Process Metallurgy and Materials Processing Science*, *50*(5), 2471–2484. https://doi.org/10.1007/s11663-019-01650-9

Spreitzer, D., & Schenk, J. (2019b). Reduction of Iron Oxides with Hydrogen—A Review. *Steel Research International*, *90*(10). https://doi.org/10.1002/srin.201900108

Sun, M., Pang, K., Barati, M., & Meng, X. (2023). Hydrogen-Based Reduction Technologies in Low-Carbon Sustainable Ironmaking and Steelmaking: A Review. *Journal of Sustainable Metallurgy*, *December 2023*. https://doi.org/10.1007/s40831-023-00772-4

Szekely, J., & El-Tawil, Y. (1976). The reduction of hematite pellets with carbon monoxide-hydrogen mixtures. *Metallurgical Transactions B*, *7*(3), 490–492. https://doi.org/10.1007/BF02652723

Tang, Q., Ma, Y., & Huang, K. (2021). Fe3O4/ZrO2Composite as a Robust Chemical Looping Oxygen Carrier: A Kinetics Study on the Reduction Process. *ACS Applied Energy Materials*, *4*(7), 7091–7100. https://doi.org/10.1021/acsaem.1c01152

Teplov, O. A. (2010). Kinetics of the low-temperature hydrogen reduction of single-crystal magnetite. *Russian Metallurgy (Metally)*, *2010*(11), 991–1000. https://doi.org/10.1134/S0036029510110017

Teplov, O. A. (2012). Kinetics of the low-temperature hydrogen reduction of magnetite concentrates. *Russian Metallurgy (Metally)*, *2012*(1), 8–21. https://doi.org/10.1134/S0036029512010132

Turkdogan, E. T., Mckewan, W. M., Zwell, L., & Bain, E. C. (n.d.). *Rate of Oxidation of Iron to Wustite in Water-Hydrogen Gas Mixtures 327 Rate of Oxidation of Iron to Wustite in Water-Hydrogen Gas Mixtures*. https://pubs.acs.org/sharingguidelines

Turkdogan, E. T., & Vinters, J. V. (1971). Gaseous reduction of iron oxides: Part I. Reduction of hematite in hydrogen. *Metallurgical and Materials Transactions B, 2*(11), 3175–3188. https://doi.org/10.1007/bf02814970

Urpelainen, S., Säthe, C., Grizolli, W., Agåker, M., Head, A. R., Andersson, M., Huang, S. W., Jensen, B. N., Wallén, E., Tarawneh, H., Sankari, R., Nyholm, R., Lindberg, M., Sjöblom, P., Johansson, N., Reinecke, B. N., Arman, M. A., Merte, L. R., Knudsen, J., … Hennies, F. (2017). The SPECIES beamline at the MAX IV Laboratory: A facility for soft X-ray RIXS and APXPS. *Journal of Synchrotron Radiation*, *24*(1), 344–353. https://doi.org/10.1107/S1600577516019056

Wagner, D., Devisme, O., Patisson, F., & Ablitzer, D. (2006). A laboratory study of the reduction of iron oxides by hydrogen. *2006 TMS Fall Extraction and Processing Division: Sohn International Symposium*, *2*, 111–120.

Wang, L., Guo, P., Kong, L., & Zhao, P. (2022). Industrial application prospects and key issues of the pure-hydrogen reduction process. *International Journal of Minerals, Metallurgy and Materials*, *29*(10), 1922–1931. https://doi.org/10.1007/s12613-022-2478-4

Wang, R. R., Zhao, Y. Q., Babich, A., Senk, D., & Fan, X. Y. (2021). Hydrogen direct reduction (H-DR) in steel industry—An overview of challenges and opportunities. *Journal of Cleaner Production*, *329*(June), 129797. https://doi.org/10.1016/j.jclepro.2021.129797

Yamashita, T., & Hayes, P. (2008). Analysis of XPS spectra of Fe 2+ and Fe 3+ ions in oxide materials. *Applied Surface Science*, *254*(8), 2441–2449. https://doi.org/10.1016/j.apsusc.2007.09.063

Yilmaz, C., Wendelstorf, J., & Turek, T. (2017). Modeling and simulation of hydrogen injection into a blast furnace to reduce carbon dioxide emissions. *Journal of Cleaner Production*, *154*, 488–501. https://doi.org/10.1016/j.jclepro.2017.03.162

Yu, D., Zhu, M., Utigard, T. A., & Barati, M. (2013). TGA kinetic study on the hydrogen reduction of an iron nickel oxide. *Minerals Engineering*, *54*, 32–38. https://doi.org/10.1016/j.mineng.2013.03.018

Yu, J., Han, Y., Li, Y., Gao, P., & Li, W. (2017). Mechanism and kinetics of the reduction of hematite to magnetite with CO–CO2 in a micro-fluidized bed. *Minerals*, *7*(11). https://doi.org/10.3390/min7110209

Zakeri, A., Coley, K. S., & Tafaghodi, L. (2025). Microstructural Evolution and Its Effect on Reaction Rate During Reduction of High-Grade Hematite Ore Pellets With Hydrogen. *Journal of Sustainable Metallurgy*. https://doi.org/10.1007/s40831-024-00990-4

Zhang, A., Monaghan, B. J., Longbottom, R. J., Nusheh, M., & Bumby, C. W. (2020). Reduction Kinetics of Oxidized New Zealand Ironsand Pellets in H2 at Temperatures up to 1443 K. *Metallurgical and Materials Transactions B: Process Metallurgy and Materials Processing Science*, *51*(2), 492–504. https://doi.org/10.1007/s11663-020-01790-3

Zhang, J., Li, S., & Wang, L. (2024). Kinetics analysis of direct reduction of iron ore by hydrogen in fluidized bed based on response surface methodology. *International Journal of Hydrogen Energy*, *49*(xxxx), 1318–1331. https://doi.org/10.1016/j.ijhydene.2023.09.243

Zuo, H. bin, Wang, C., Dong, J. ji, Jiao, K. xin, & Xu, R. sheng. (2015). Reduction kinetics of iron oxide pellets with H2 and CO mixtures. *International Journal of Minerals, Metallurgy and Materials*, *22*(7), 688–696. https://doi.org/10.1007/s12613-015-1123-x

Original publications

- I Heidari, A., Niknahad, N., Iljana, M., & Fabritius, T. (2021). A review on the kinetics of iron ore reduction by hydrogen. *Materials*, *14*(24), 7540. https://doi.org/10.3390/ma14247540
- II Heidari, A., Ghosalya, M. K., Alaoui Mansouri, M., Heikkilä, A., Iljana, M., Kokkonen, E., Huttula, M., Fabritius, T., & Urpelainen, S. (2024). Hydrogen reduction of iron ore pellets: A surface study using ambient pressure X-ray photoelectron spectroscopy. *International Journal of Hydrogen Energy*, *83*, 148–161. https://doi.org/10.1016/j.ijhydene.2024.08.094
- III Heidari, A., Heikkilä, A., Iljana, M., & Fabritius, T. (2024). A comparison between the reduction behavior of DRI and BF pellets in H_2 and CO atmospheres. *Journal of Sustainable Metallurgy*, *10*(4), 2068–2084. https://doi.org/10.1007/s40831-024-00951-x
- IV Heidari, A., Ilmakangas, T., Pöyhtäri, S., Heikkinen, E. P., Sulasalmi, P., & Fabritius, T. (In press). The influence of water vapor on hydrogen reduction of iron ore pellets. *Ironmaking & Steelmaking*.

Original publications are not included in the electronic version of the dissertation.

---

[1] https://creativecommons.org/licenses/by/4.0/

ACTA UNIVERSITATIS OULUENSIS

SERIES C TECHNICA

997. Karioja, Konsta (2025) Signal processing and feature extraction for automated machine diagnostics : methodology and experiments
998. Valente da Silva, Matheus (2025) Distributed learning methods in machine-type communications
999. Jiang, Chuqing (2025) Magnesium-based glasses prepared by sol-gel processing for use as supplementary cementitious materials
1000. Sadeghi Vilni, Saeid (2025) Status update optimization for information freshness and real-time tracking
1001. Haapala, Anne (2025) Kinestetiikan koulutusintervention hyödyt omaishoitajille ja -hoidettaville kotikontekstissa
1002. Rajapakshalage, Dhanushka Nalin Jayaweera (2025) 5G-Advanced network optimization : AI/ML and sensing-driven beam management with energy optimization
1003. Varanka, Tuomas (2025) Uncovering the subtle details of faces
1004. Saranya, Muthusamy (2025) Carbon nanotube-based scaffold for cell modulation
1005. Tesfamariam, Axumawit Tequam (2025) The development of tools and methods for the evaluation of the physical integrity of sewage networks : a focus on physicochemical and hydrological approaches
1006. Li, Junhao (2025) Human evaluation and tool development for online content credibility
1007. Ma, Mengyuan (2025) Beamforming designs for low-power transceiver structures in large-scale MIMO systems
1008. Välikangas, Juho (2025) Modification of lithium nickel oxide cathode material
1009. Hietanen, Mikko (2025) Design of millimeter-wave RF front-ends for phased array communication systems on CMOS SOI
1010. Savic, Marko (2025) Remote photoplethysmography : advancing robustness, privacy and security
1011. Kokko, Maria (2025) Recovery of vanadium from metallurgical industry side streams : leaching and crystallization studies
1012. Rajna, Zalán (2025) Tracking neuronal and cardiovascular impulses in MR-encephalography

Book orders:
Virtual book store
https://verkkokauppa.omapumu.com/fi/

UNIVERSITY OF OULU P.O. Box 8000 FI-90014 UNIVERSITY OF OULU FINLAND

ACTA UNIVERSITATIS OULUENSIS

UNIVERSITY OF OULU

ISBN 978-952-62-4544-7 (Paperback)
ISBN 978-952-62-4545-4 (PDF)
ISSN 0355-3213 (Print)
ISSN 1796-2226 (Online)